Instantaneous deformation and kinematics of the India–Australia Plate

Matthias Delescluse[1,3] and Nicolas Chamot-Rooke[1,2]

[1]*Laboratoire de géologie, Ecole Normale Supérieure, Paris, France*
[2]*CNRS UMR 8538. E-mail: rooke@geologie.ens.fr*
[3]*Université Paris XI, France. E-mail: delesclu@geologie.ens.fr*

SUMMARY

Active intraplate deformation of the India–Australia Plate is now being captured by far-field global positioning system (GPS) measurements as well as measurements on a few islands located within the deforming zone itself. In this paper, we combine global and regional geodetic solutions with focal mechanisms of earthquakes to derive the present-day strain field of the India–Australia Plate. We first compile an updated catalogue of 131 Indian intraplate earthquakes ($M > 5$) spanning the period between the two Asian mega earthquakes of Assam 1897 and Sumatra 2004. Using Haines and Holt's numerical approach applied to a fully deformable India–Australia Plate, we show that the use of GPS data only or earthquakes data only has severe drawbacks, related, respectively, to the small number of stations and the incompleteness of the earthquakes catalogue. The combined solution avoids underestimation of the strain inherent to the Kostrov summation of seismic moments and provides details that cannot be reached by pure GPS modelling. We further explore the role of heterogeneity of the India–Australia Plate and find that the best model, in terms of geodetic vectors fit, relative distribution of strain, style and direction of principal strain from earthquakes, is obtained using the surface heat-flow as a proxy for rheological weakness of the oceanic lithosphere. The present-day deformation is distributed around the Afanasy Nikitin Chain in the Central Indian Basin (CIB)—where it is almost pure shortening—and within the Wharton Basin (WB) off Sumatra—where it is almost pure lateral strike-slip. The northern portion of NinetyEast ridge (NyR) appears as a major discontinuity for both strain and velocity. The new velocity field gives an India/Australia rotation pole located at 11.3°S, 72.8°E ($-0.301°$ Myr^{-1}) overlapping with previous solutions, with continental India moving eastward at rates ranging from 13 mm yr^{-1} (southern India) to 26 mm yr^{-1} (northern India) with respect to Australia. Taking into account the intraplate velocity field in the vicinity of the Sumatra trench, we obtain a convergence rate of 46 mm yr^{-1} towards N18°E at the epicentre of the 2004 Aceh megaearthquake. The predicted instantaneous shortening in the CIB and WB and extension near Chagos-Laccadive are in good agreement with the finite deformation measured from plate reconstructions and seismic profiles, suggesting a continuum of deformation since the onset of intraplate deformation around 7.5–8 Ma. Since no significant change in India convergence is detected at that time, we suggest that the intraplate deformation started with the trenchward acceleration of Australia detaching from India along a wide left-lateral oceanic shear band activating the NyR line of weakness as well as north–south fracture zones east of it. The predicted total amount of left lateral finite strain along these faults is in the range 110–140 km.

Key words: earthquakes, India–Eurasia collision, intraplate deformation, global positioning system (GPS), plate tectonics, strain modelling.

1 INTRODUCTION

Ninetyeast ridge (hereafter NyR) has long been recognized as a potential kinematic boundary between India and Australia (Le Pichon 1968, p. 3676). In the early global kinematic models, strike-slip motion along the ridge itself—or along nearby fracture zones—was considered as one possible solution to the problem of non-closure of the Africa/Antarctica/India–Australia Plate circuit (Minster

& Jordan 1978). Stein & Okal (1978) summed up seismic moment of historical earthquakes release along the NyR and estimated as much as 20 mm yr^{-1} of sinistral shear. However, their two plate model failed to explain the widespread seismicity in the Indian equatorial zone, as well as finite compressive deformation observed in seismic profiles at large distance from the ridge. Wiens *et al.* (1985) introduced the diffuse boundary zone concept, a wide zone of deformation extending from the western flank of the NyR to the Chagos Laccadive Ridge, some 2000 km west of it. East of NyR, the Wharton Basin (hereafter WB) was considered as part of rigid Australia, NyR still acting as the eastern boundary of a highly deformed zone. Re-evaluation of the historical seismic moment release scaled the maximum motion along the NyR down to a few millimetres per year only (DeMets *et al.* 1988; Petroy & Wiens 1989). This, along with the abundant historical seismicity recorded in the WB, led to the present-day definition of the diffuse boundary zone: a nearly equatorial region spreading from Chagos Laccadive to the WB and Sumatra trench. Gordon *et al.* (1990) and DeMets *et al.* (1988) showed that this model is compatible with the style of focal mechanisms: N–S extension near Chagos Laccadive, N–S compression in the Central Indian Basin (hereafter CIB), NW–SE compression in the WB. The role of the NyR in controlling the deformation is minimized, and the Central and eastern Indian Ocean lithosphere deform equally west and east of it.

The boundary role played by NyR was re-evaluated in two studies, one based on strain modelling (Tinnon *et al.* 1995) and the other based on a marine survey (Deplus *et al.* 1998). Tinnon *et al.* (1995) computed the strain rate field in the diffuse deformation zone using Kostrov summation of seismic moments (Kostrov 1974) and Haines & Holt method (Haines & Holt 1993; Haines *et al.* 1998; Holt & Haines 1995) to derive a continuous horizontal velocity field. In their modelled strain rate field, strike-slip motion in the WB is predicted only if NyR strongly localizes deformation. Their interpretation is that the ridge must be weak compared to the WB and the CIB. Seismic profiles collected by Deplus *et al.* show that recent deformation is not limited to the NyR itself. Deformation in the WB consists in the re-activation of N–S palaeotransform faults that are parts of a fossil spreading ridge system (Deplus *et al.* 1998; Deplus 2001). Their conclusion is that the NyR acts as a major boundary for the style of deformation: pure compression west of it, pure strike-slip east of it. Indeed seismic profiles collected to the west of the ridge (Bull 1990; Bull & Scrutton 1992; Chamot-Rooke *et al.* 1993; Van Orman *et al.* 1995) show mainly shortening on E–W thrust faults, even close to the ridge (Krishna *et al.* 1998), with marginal strike-slip activity. Deformation occurs almost exclusively as strike-slip in the WB.

In this paper, we propose a re-evaluation of the instantaneous strain-rate field using an updated catalogue of historical earthquakes and incorporating GPS constraints from various regional studies. At variance with the global model of Kreemer *et al.* (2003), our model uses a fully deformable Indian plate, without any *a priori* constraint on the geometry of the zone of diffuse deformation. Although only few stations are available, we show that they act as strong far-field boundary conditions. Using Haines and Holt approach, we derive successively two strain-rate fields: one using the Kostrov summation of seismic moments and the other based on GPS velocities only. We then discuss a model that incorporates both earthquakes and GPS data, and show that some of the drawbacks inherent to the use of earthquakes only or GPS only are minimized in our best model. Spatial rheological variations of the Indian oceanic lithosphere are also introduced using the age of the oceanic lithosphere and the sur-face heat flow. Finally, our results are discussed in terms of regional kinematics and dynamics.

2 SEISMICITY AND GPS CONSTRAINTS ON THE INSTANTANEOUS DEFORMATION

2.1 Earthquake data

In an attempt to have the best possible spatial and temporal image of the seismicity, we compiled a catalogue of 131 Indian (continental and oceanic) intraplate earthquakes (Table 1) which is merely an extension of the initial compilation by Tinnon *et al.* (1995). The new catalogue gathers earthquakes focal mechanisms from various published sources, each focusing on different zones of the Indian Plate. It includes historical and instrumental seismicity for the time period between the two largest earthquakes that have occurred around India: the Mw8.1 Assam earthquake (1897) and the Mw9.3 Sumatra earthquake (2004). Actually some of the aftershocks of the recent great Sumatra earthquake have been included in our calculations. We did not keep earthquakes with magnitude below five to avoid unreliable focal mechanisms. A clear limitation of this new catalogue is that several large historical earthquakes could not be included since they lack focal mechanisms.

Fig. 2 shows the focal mechanisms of all earthquakes in the catalogue. At variance with previous strain models, our catalogue includes not only the Indian Ocean, but also continental India, since deformation may not be limited to the oceanic domain, and the Bay of Bengal. The rationale is that stress building in the Central Indian Ocean necessarily implies stress transmission across continental India (Bilham *et al.* 2003). The Shillong plateau is a spectacular example of the high level of seismicity and strong localized deformation affecting continental India. Bilham & England (2001), by re-measuring the 1862 British triangulation network, showed that the 1897 Assam earthquake corresponds to a slip of 18 ± 7 m on a buried thrust fault. This fault bounds the northern Shillong plateau, thus interpreted as a crustal-scale pop-up structure. The plateau shows similarities with intraplate deformation found at distance from the subduction trenches, interpreted as the combined result of plate bending stress and regional compressive stress (Bilham *et al.* 2003; Chamot-Rooke & Le Pichon 1989). We thus consider that the seismicity of the Shillong plateau is of intraplate type rather than being related to some kind of southern prolungation of Himalayan faults as formerly assumed. In any case, stresses are transferred from the Himalayan thrust to the lithosphere of the Bay of Bengal. On the other side of continental India, the recent Bhuj earthquake (*Ms* = 8.0, 2001/01/27), along with earthquakes in peninsular India and Bengal Bay, all have N–S *P*-axis, suggesting that they do relate to the intraplate deformation found further south in the oceanic domain.

The highest level of seismicity is within the Indian Ocean. Seismicity is high along NyR itself and east of it, consistent with the fact that deformation is not restricted to the CIB. West of the ridge, in the CIB, seismicity is associated with E–W thrust faults imaged by seismic profiles (Bull 1990; Bull & Scrutton 1992; Chamot-Rooke *et al.* 1993; Van Orman *et al.* 1995; Krishna *et al.* 1998; Krishna & Gopala Rao 2000). A few fractures zones (probably re-activation of palaeotransform faults) seem to be active too, especially near the Afanasy Nikitin seamount chain. The westernmost portion of the diffuse deformation zone, Chagos Laccadive ridge, is affected by abundant extensive seismicity (Wiens 1986) concentrated in a very

Table 1. Catalogue of 131 Indian intraplate earthquakes ($M > 5$).

Date	Lonitude	Latitude	M	Moment	Strike	Dip	Rake	Depth	Source	Notes
Chagos Laccadive Ridge										
1944/02/29	76.0	0.5	7.2	1.4×10^{20}	115	50	60	10	(15)	
1957/10/02	69.7	−6.3	5.7	1.4×10^{18}	35	90	180	14	(15)	NR
1965/09/12	70.746	−6.475	6	4.9×10^{18}	250	55	−120	18	(4)	
1967/11/10	71.293	−6.014	5.2	3.0×10^{17}	234	76	−169	18	(4)	$M = Mb$
1967/11/11	71.301	−6.082	5.2	3.7×10^{17}	264	50	−99	17	(4)	
1968/03/02	71.381	−6.14	5.4	7.7×10^{17}	284	52	−80	13	(4)	
1970/03/31	69.678	−3.784	5.5	1.5×10^{18}	248	62	−143	12	(14)	
1970/04/25	69.773	−6.339	5.1	3.5×10^{17}	320	78	−30	15	(14)	
1973/11/17	69.915	−1.583	5.5	7.4×10^{17}	278	55	−38	19	(14)	
1978/05/20	69.656	−3.465	4.9	1.89×10^{17}	148	81	8	15	(1)	
1981/12/12	70.172	4.88	5.1	3.09×10^{17}	37	17	−78	15	(1)	
1983/11/30	72.065	−6.835	7.5	4.05×10^{20}	293	35	−52	10	(1)	
1983/12/01	71.745	−6.685	5.6	4.95×10^{17}	310	46	−43	10	(1)	
1983/12/01	71.745	−6.685	5.2	4.76×10^{16}	93	40	−99	17	(1)	
1983/12/01	71.745	−6.685	5.3	5.01×10^{17}	71	41	−128	10	(1)	
1983/12/02	71.058	−6.536	4.9	2.14×10^{17}	131	41	−70	18	(1)	
1983/12/03	71.393	−6.478	6.3	3.13×10^{18}	303	37	−47	12	(1)	
1983/12/12	71.423	−6.566	5.2	2.36×10^{17}	92	44	−115	10	(1)	
1983/12/20	71.279	−6.702	5.4	1.25×10^{17}	100	46	−135	10	(1)	
1983/12/27	72.345	−6.836	5.2	1.81×10^{17}	284	38	−59	10	(1)	
1983/12/29	71.464	−6.786	5.2	2.45×10^{17}	299	39	−60	10	(1)	
1984/04/05	74.843	0.163	5.1	7.14×10^{16}	297	68	166	10	(1)	
1984/04/26	71.463	−6.785	5.2	2.45×10^{17}	299	39	−60	10	(1)	
1984/11/18	74.839	0.187	5.1	7.14×10^{16}	297	68	166	10	(1)	
1987/07/03	72.221	−6.758	5.4	3.78×10^{17}	48	25	−125	15	(1)	
1988/06/10	72.219	−6.878	5.2	3.09×10^{17}	112	10	−69	15	(1)	
1989/03/23	72.291	−6.862	5.2	3.09×10^{17}	13	12	−159	15	(1)	
1997/11/05	73.749	−2.141	5.3	2.39×10^{17}	195	68	−5	15	(1)	
Central Indian Basin										
1913/01/19	88.0	1.0	7	4.3×10^{19}	79	44	96	?	(3)	
1970/10/10	86.124	−3.606	6.3	4.1×10^{18}	19	89	-2	27	(4)	
1970/10/10	86.126	−3.606	6.3	2.1×10^{18}	32	73	21	39	(4)	
1972/11/24	85.336	11.613	5.2	3×10^{17}	254	52	76	27	(5)	
1973/08/30	84.292	7.11	5.8	3.7×10^{17}	290	52	118	27	(5)	
1978/08/03	84.185	−0.965	5.6	7.14×10^{17}	64	35	79	42.8	(1)	
1981/04/12	85.396	8.203	5.2	1.84×10^{17}	340	73	−177	15	(1)	
1983/08/21	87.503	3.278	5.5	1.64×10^{17}	132	23	146	10.1	(1)	
1987/09/22	84.346	−0.777	5	9.67×10^{16}	307	90	180	15	(1)	
1989/06/20	86.954	−3.789	4.6	1.13×10^{17}	284	31	139	15	(1)	
1989/10/15	82.42	−0.213	5.1	8.77×10^{16}	299	90	−180	15	(1)	
1991/01/13	84.539	−2.863	5.4	5.93×10^{17}	48	33	22	15	(1)	
1991/05/13	82.791	−3.452	5.5	1.02×10^{18}	41	27	28	25	(1)	
1992/01/11	86.928	9.251	5	3.51×10^{17}	296	48	136	17.1	(1)	
1992/08/16	84.879	−3.059	5.7	1×10^{17}	90	33	72	34	(1)	
1995/07/27	79.21	−12.598	5.9	1.07×10^{18}	275	33	135	18	(1)	
1999/03/29	87.168	−4.053	5.5	6.36×10^{17}	118	47	174	15	(1)	
2001/09/02	82.452	0.912	5.8	1.39×10^{18}	280	64	170	15	(1)	
Ninetyeast ridge										
1928/03/09	88.8	−2.954	7.7	4.1×10^{20}	194	84	−9	29	(11)	
1939/03/21	89.401	−1.285	7.2	2×10^{20}	166	82	57	?	(12)	
1964/05/25	88.824	−9.096	6	9.6×10^{17}	177	87	5	17	(5)	
1973/04/07	91.28	6.983	6.6	2.5×10^{18}	34	84	−4	13	(5)	
1973/04/07	91.28	6.983	6.6	8.3×10^{18}	20	87	9	6	(5)	
1979/10/16	91.167	6.382	5.1	2.4×10^{17}	14	76	−7	16	(1)	
1980/01/28	88.812	−3.397	5.2	2.57×10^{17}	280	83	178	15	(1)	
1980/03/11	88.816	−3.365	5.3	1.7×10^{17}	18	62	−10	12	(11)	
1981/12/02	88.364	−15.738	5.5	6.19×10^{17}	195	52	33	10	(1)	
1989/02/10	92.228	6.305	5.3	6.2×10^{17}	291	71	−176	15	(1)	
1996/04/18	87.201	−16.127	5	1.95×10^{17}	169	87	0	15	(1)	$M = Mb$
1999/05/25	90.106	3.699	5.1	2.2×10^{17}	117	82	−178	22.2	(1)	
2005/07/24	91.850	7.950	7.5	8.88×10^{19}	29	83	−18	17	(1)	NR

Table 1. (*Continued.*)

Date	Lonitude	Latitude	M	Moment	Strike	Dip	Rake	Depth	Source	Notes
1999/11/15	88.929	−1.382	6.9	3.3×10^{19}	12	76	−11	15	(1)	
1999/11/28	88.933	−1.307	5	1.42×10^{17}	7	76	10	15	(1)	
1999/11/29	88.958	−1.302	6.4	4.5×10^{18}	22	77	−2	15	(1)	
2000/01/28	89.04	−1.358	5.2	2.27×10^{17}	17	79	−1	15	(1)	

Wharton Basin

Date	Lonitude	Latitude	M	Moment	Strike	Dip	Rake	Depth	Source	Notes
1949/01/23	93.0	−11.0	6.8	1.3×10^{19}	85	80	−165	15	(11)	
1955/03/23	91.762	−9.207	6.5	1.7×10^{19}	55	78	118	32	(11)	
1965/10/31	95.181	−14.24	5.4	6.1×10^{17}	165	68	9	24	(5)	
1971/06/26	96.843	−5.215	6.4	5.4×10^{18}	14	67	19	29	(5)	
1979/07/17	98.663	−4.488	5.2	3.82×10^{17}	247	48	138	29	(1)	
1979/09/29	94.172	1.161	6.8	2.21×10^{19}	284	88	−179	38.8	(1)	
1983/03/03	100.656	−6.16	5.4	1.93×10^{17}	9	58	−25	42.1	(1)	
1987/03/15	91.559	−10.364	4.8	2.25×10^{17}	224	19	105	15	(1)	
1989/09/29	98.005	−15.888	5.1	1.15×10^{17}	139	29	15	15	(1)	
1989/12/17	92.161	−8.453	5.3	7.62×10^{17}	259	46	158	15	(1)	
1990/01/06	92.932	−10.644	5.5	1.17×10^{18}	8	25	52	15	(1)	
1990/10/15	92.234	−2.21	6.5	1.35×10^{19}	19	70	−2	23	(1)	
1992/06/02	92.815	−16.122	5.4	6.82×10^{17}	254	90	−180	15	(1)	
1992/06/02	92.815	−16.122	5.8	2.53×10^{18}	169	70	21	15	(1)	
1995/11/08	95.012	1.82	6.9	2.65×10^{19}	192	77	0	29.6	(1)	
1998/10/31	98.678	−6.281	5.2	3.36×10^{17}	89	79	−178	15	(1)	
2000/06/18	97.328	−13.896	7.8	5.53×10^{20}	337	77	17	21	(2)	$M = Mw$
2000/06/18	97.33	−13.9	7.5	1.82×10^{20}	206	40	30	24	(2)	$M = Mw$
2000/06/20	97.486	−14.144	5.6	4.94×10^{17}	257	90	−180	15	(1)	
2000/08/01	93.124	4.048	5	1.08×10^{17}	192	86	4	34.9	(1)	
2001/09/07	97.224	−13.193	5.8	8.63×10^{17}	232	36	110	15	(1)	
2004/07/10	94.77	−8.92	5.2	2.94×10^{17}	188	76	43	12	(1)	NR
2005/01/01	92.20	4.99	6.5	1.05×10^{19}	110	80	−177	12	(1)	NR
2005/02/15	92.16	1.82	5.5	1.66×10^{17}	13	86	−26	12	(1)	NR

Shillong Plateau

Date	Lonitude	Latitude	M	Moment	Strike	Dip	Rake	Depth	Source	Notes
1897/06/12	91.0	25.5	8.1	1.28×10^{21}	290	57	76	30	(6)	$M = Mw$. NR
1947/07/29	93.73	28.63	7.3	1.50×10^{20}	270	5	90	?	(13)	NR
1950/08/15	96.76	28.38	8.6	9.00×10^{21}	265	12	90	?	(13)	NR
1963/06/19	92.06	24.97	?	?	57	80	42	52	(10)	
1963/06/21	92.09	25.13	?	?	238	88	−70	38	(10)	
1964/02/18	91.24	27.39	5.3	?	302	40	90	16	(8)	$M = Mb$
1968/06/12	91.94	24.83	5.3	?	132	60	135	41	(10)	$M = Mb$
1968/08/18	90.62	26.42	5.1	?	90	60	90	29	(10)	$M = Mb$
1968/12/27	91.61	24.12	5.1	?	140	72	138	29	(10)	$M = Mb$
1971/02/02	91.66	23.71	5.4	?	119	36	90	46	(10)	$M = Mb$
1971/07/17	93.15	26.41	5.4	2.6×10^{17}	79	60	46	36	(10)	$M = Mb$
1977/10/13	93.30	23.49	5.4	1.6×10^{17}	145	41	−171	61	(1)	$M = Mw$
1984/12/30	92.89	24.64	5.5	1.3×10^{18}	350	45	122	?	(10)	$M = Mw$
1986/08/02	93.00	23.91	5	1.46×10^{17}	224	62	−15	33	(1)	
1986/02/19	91.14	25.14	5.3	1.08×10^{17}	340	50	180	18	(1)	
1988/02/06	91.51	24.67	5.8	6.7×10^{17}	239	76	9	31	(1)	
1988/08/06	95.12	25.14	7.2	8.9×10^{19}	284	45	55	100	(7)	NR
1989/04/13	92.41	24.40	5	1.7×10^{17}	291	6	20	33	(1)	
1989/06/12	89.75	21.83	5.1	5.8×10^{17}	354	67	164	15	(1)	
1996/11/19	92.64	24.54	5	1.3×10^{17}	102	34	59	53	(1)	
1997/05/08	92.23	24.90	5.6	8.57×10^{17}	78	68	4	35	(1)	

Western India

Date	Lonitude	Latitude	M	Moment	Strike	Dip	Rake	Depth	Source	Notes
1991/11/08	70.658	26.358	5	1.37×10^{17}	56	43	46	22	(1)	
2001/01/26	70.234	23.394	8	3.43×10^{20}	298	39	136	19.8	(1)	
2001/01/28	70.541	23.466	5.5	5.22×10^{17}	286	43	111	15	(1)	
2001/01/28	70.422	23.308	5.4	1.28×10^{17}	281	24	158	15	(1)	$M = Mw$
2001/02/19	70.137	23.522	5.1	1.45×10^{17}	254	42	78	15	(1)	

Peninsular India

Date	Lonitude	Latitude	M	Moment	Strike	Dip	Rake	Depth	Source	Notes
1964/04/15	88.074	21.729	5.2	?	291	18	90	36	(9)	$M = Mb$
1967/03/27	80.145	15.592	5.2	?	278	25	90	17	(9)	$M = Mb$

Table 1. (*Continued.*)

Date	Lonitude	Latitude	M	Moment	Strike	Dip	Rake	Depth	Source	Notes
1967/12/10	73.774	17.389	6.6	8.91×10^{18}	206	51	−20	12	(9)	$M = Mw$
1969/04/13	80.679	17.839	5.7	3.98×10^{17}	307	8	90	33	(9)	
1969/10/24	72.44	24.796	4.9	?	128	55	135	15	(9)	M = Mb
1970/03/23	72.975	21.582	5.2	?	275	45	53	3	(9)	M = Mb
1988/08/21	86.61	26.78	6.6	2.31×10^{19}	230	23	2	34.7	(7)	NR
1993/09/29	76.516	18.079	6.3	2.21×10^{18}	134	47	112	15	(1)	
1997/05/21	80.121	23.066	5.6	5.83×10^{17}	283	26	129	38	(1)	
Bengal Bay										
1976/06/23	88.63	21.259	5	?	256	10	90	34	(8)	$M = Mb$
1982/04/08	86.353	18.531	5.2	7.6×10^{16}	66	42	90	36	(8)	$M = Mw$
1982/07/04	90.59	19.52	5.2	2.68×10^{17}	240	73	0	29.4	(1)	
1985/07/01	87.249	18.404	5.5	1.99×10^{17}	137	10	90	20	(8)	$M = Mw$
1989/06/12	89.746	21.829	5.1	5.8×10^{17}	354	67	164	15	(1)	
1992/07/09	90.004	21.056	5.3	1.11×10^{17}	79	59	13	30	(1)	$M = Mw$
1997/11/21	92.688	22.241	6.1	1.55×10^{18}	163	37	168	54	(1)	
2003/07/26	92.31	22.85	5.5	3.53×10^{17}	338	32	82	15	(1)	NR
2003/07/27	92.34	22.83	5.4	1.69×10^{17}	2	16	88	15	(1)	$M = Mw$, NR

M is Ms unless specified in 'Notes' column, moments are given in N m, depth in km. Positions of earthquakes are those relocated by (Engdahl *et al.* 1998) except if NR appears in 'Notes' column. Sources are (1), Harvard Centrod Moment Tensor Catalogue; (2), (Abercrombie *et al.* 2003); (3), (Bergman *et al.* 1984); (4), (Bergman & Solomon 1984); (5), (Bergman & Solomon 1985); (6), (Bilham & England 2001); (7), (Bilham *et al.* 2003); (8), (Biswas & Majumdar 1997); (9), (Chandra 1977); (10), (Chen & Molnar 1990); (11), (Petroy & Wiens 1989); (12), (Stein & Okal 1978); (13), (Triep & Sykes 1997); (14), (Wiens & Stein 1984) and (15), (Wiens 1986).

narrow area. DeMets *et al.* (1994b) demonstrate, with aeromagnetic data and azimuths of the Karlsberg Ridge transform faults, that this area corresponds to the loose location of the Australia/Africa/India 'triple junction'.

In the WB, most of the earthquakes have a strike-slip focal mechanism with NW–SE *P*-axis, with a few thrust mechanisms. Strike-slip faulting also occurs in portions of the Indian lithosphere already engaged in the Sumatra subduction. Abercrombie *et al.* (2003) decomposed the 2000 June 4 Enggano earthquake in the Sumatra trench in two subevents. The first subevent is a left-lateral strike-slip, with a typically intraplate NW–SE *P*-axis, while the second one is a subduction thrust. Complex interactions thus exist between intraplate and subduction stresses in the Sumatra-trench. Similar interactions occurred following the recent 2004 December 26 Aceh megathrust earthquake. Several of the largest aftershocks have a NW–SE trending *P*-axis, suggesting an intraplate origin. We rejected four of these, located in the trench, or close to it, because they did not have strong enough double-couple components. However, we did include three other aftershocks (2005/01/01, $M = 6.5$; 2005/02/15, $M = 5.5$; 2005/05/24, $M = 7.5$) located quite far west of the trench and with much stronger double-couple components. They correspond to pure left lateral strike-slip motion on roughly N–S shear planes.

The most important addition to Tinnon *et al.*'s (1995) catalogue is the large magnitude Cocos earthquake. Abercrombie *et al.* (2003) decomposed the Cocos island earthquake (2000/06/18, $M = 7.8$, 97.33°E, 13.9°S) in two subevents, one with a strike-slip focal mechanism, the other with a compressive one, suggesting complex seismic partitioning onto N–S sinistral shear planes and NE–SW thrust planes. This large event suggests that the southern limit of the deformation may be located quite far south in the WB compared to the CIB: the southern limit of the diffuse boundary zone, formerly defined at 10°S by Tinnon *et al.* (1995), should be extended at least to 15°S in the WB. We thus choose in our models to authorize deformation everywhere in the Indian plate for latitudes above 20°S. The expectation is that we now have enough constraints—including seis-

micity and far-field GPS velocities—to reveal where deformation occurs as an output of the models.

2.2 Geodetic data

In order to introduce as much kinematic constraints as possible and to cover the largest area, we use GPS velocities from four studies. The first one is the worldwide solution of Heflin at Nasa (solution 2004.2 at http://sideshow.jpl.nasa.gov/mbh/series.html). The three others are either regional—the recent Asia solutions by Socquet *et al.* (2006) and by Banerjee (2005)—or local—the Indian solution of Paul *et al.* (2001). The first three solutions were originally given in the ITRF2000 frame, while Paul's solution is in an Indian reference frame.

We selected 13 GPS velocities from Socquet (Table 2), including four southern Nepalese stations (BHAI, MAHE, NEPA and SIMR)

Table 2. GPS velocities from Socquet *et al.* (2006) in mm yr^{-1}, ITRF2000 reference frame.

Stations	Latitude	Longitude	V_E	V_N	σ_{V_E}	σ_{V_N}
BHAI	27.51	83.42	37.04	34.32	0.94	0.37
COCO[a]	−12.19	96.83	48.45	47.18	0.23	0.09
DARW	−12.84	131.13	35.74	56.94	0.34	0.12
HYDE	17.42	78.55	41.44	34.66	0.65	0.23
IISC	13.02	77.57	40.02	33.32	0.19	0.08
KARR	−20.98	117.10	37.64	56.41	0.22	0.10
MORE[a]	−9.43	147.19	34.15	51.41	1.32	0.40
NEPA	28.13	81.57	38.28	35.67	0.80	0.32
PERT	−31.80	115.89	38.48	57.23	0.16	0.10
SIMR	27.17	84.98	40.57	32.60	1.17	0.48
TIDB	−35.40	148.98	18.49	55.05	0.10	0.08
YAR1	−29.05	115.35	38.56	56.10	0.15	0.09
MAHE	28.96	80.15	37.17	33.59	0.81	0.31

Bold station names are within our deformable grid.
[a]Socquet (2003).
Uncertainties are 1σ errors.

Table 3. GPS velocities from heflin *et al.* (2004.2) in mm yr^{-1}, ITRF2000 reference frame.

Stations	Latitude	Longitude	V_E	V_N	σ_{V_E}	σ_{V_N}
TID1	−35.39	148.98	17.80	53.87	0.10	0.06
STR1	−35.31	149.01	17.93	54.60	0.11	0.07
TID2	−35.39	148.98	17.95	54.69	0.05	0.03
CANB	−35.39	148.98	18.03	54.84	0.05	0.02
CEDU	−31.86	133.81	28.85	57.38	0.09	0.05
TOW2	−19.26	147.05	28.33	53.88	0.09	0.05
ALIC	−23.67	133.88	31.56	57.06	0.10	0.05
STR2	−35.31	149.01	18.74	52.40	4.40	2.82
NOUM	−22.27	166.41	19.96	44.76	0.08	0.04
HOB2	−42.80	147.43	14.27	55.70	0.04	0.02
AUCK	−36.60	174.83	3.35	39.07	0.04	0.02
PERT	−31.80	115.88	39.28	57.13	0.04	0.02
JAB1	−12.65	132.89	35.02	56.88	0.11	0.05
YARR	−29.04	115.34	37.79	56.69	1.07	0.57
YAR2	−29.04	115.34	38.10	56.52	0.12	0.06
YAR1	−29.04	115.34	39.88	56.15	0.05	0.03
KARR	−20.98	117.09	37.76	56.57	0.10	0.05
NNOR	−31.04	116.19	36.07	56.51	0.82	0.45
DARW	−12.84	131.13	35.26	55.20	0.12	0.06
COCO	−12.18	96.83	44.08	49.19	0.11	0.05
DGAR	−7.27	72.37	45.68	30.95	0.11	0.04
MALD	4.18	73.52	45.06	31.75	1.15	0.41
IISC	13.02	77.57	40.23	33.72	0.07	0.02

Bold station names are within our deformable grid.
Uncertainties are 1σ errors.

which seem to be unaffected by elastic coupling at the frontal Himalayan thrust (see discussion in Socquet *et al.* (2006)). Other stations from Socquet *et al.* include two peninsular Indian stations (IISC and HYDE) plus one station in the deformed zone (COCO station). The latter is particularly important, since it can potentially introduce kinematic constraint near the area of the 2000/06/18 $M = 7.8$ Cocos island's earthquake. The six last stations from Socquet are Australian stations (Socquet 2003).

We also extracted 23 GPS velocities (Table 3) from Heflin *et al.* (2004.2). IISC, COCO and some of the 19 Australian stations overlap with the study by Socquet *et al.*. Australian velocities are similar in both studies, since residuals are small with respect to their ITRF2000 values. Heflin's time-series at station COCO reveal 1 cm latitudinal and 3 cm longitudinal coseismic motion for the large 2000 June earthquake, which occurred in the middle of the 8 yr long recording period (1996–2004). Corrections for coseismic motion have been applied in both studies. DGAR (Diego-Garcia) and MALD (Maldives islands) stations are particularly well located to catch extension near Chagos Laccadive. Velocities derived from both studies are plotted in Fig. 1 in an Australian reference frame. The result clearly shows India moving significantly eastward with respect to Australia. We see that velocity at COCO station is different for Socquet and Heflin. The difference may be due to the fact that Socquet does not use the full recording period but only parts of it. Accordingly, Socquet's COCO velocity has a larger error ellipse and thus will have less weight in our models than the velocity of COCO by Heflin.

We also use 13 vectors extracted from Paul *et al.* (2001) study, originally given in the Indian reference frame (Table 4), all measured between 1997 and 1999. Paul *et al.*'s solution includes GPS station SHIL where a 6.3 ± 3.8 mm yr^{-1} southward motion of the Shillong plateau with respect to India (Fig. 2) was detected. This station puts strong kinematic constraint on the Assam region as well as far-field

constraints on the Bay of Bengal. Paul *et al.* computed a significant instantaneous shortening rate of $6.5 \cdot 10^{-9}$ yr^{-1} within continental India, which is one to two orders of magnitude greater than the 1 to $3 \cdot 10^{-10}$ yr^{-1} rate they obtained by summing instrumental seismicity. They attribute the difference to the incompleteness of the seismicity catalogue. The true level of deformation of continental India thus remains questionable, the short period of GPS measurement in Paul's study causing large uncertainties.

Finally, we added a more recent regional solution by Banerjee (2005) (Table 5) which seems to have a better accuracy than the older solutions. Consequently, we assigned a larger weight to this solution in our inversion. Only IISC and SHIL are present in both studies. In total, we use 58 GPS vectors: 25 belong to rigid Australia, the remaining are within our deformable grid.

3 INSTANTANEOUS STRAIN-RATE FIELD MODELS

3.1 Kostrov summation of seismic moments

A common way to obtain the present-day strain-rate field is to sum the seismic moments as defined by Kostrov (1974). Following Tinnon *et al.* (1995) we use Haines & Holt method to compute the average directions and amplitudes of the strain rate in each cell of a deforming grid. The $3° \times 3°$ grid cell size is scaled to the major structures of the Indian ocean, keeping computing time decent. The grid is also shaped to fit the NyR morphology. In this first set of runs, the grid is limited to the oceanic domain to better compare the effect of the introduction of the recent earthquakes absent in Tinnon *et al.* (1995), in particular the two large earthquakes that have shocked NyR (1999/11/15, $M = 6.9$) and the WB (2000/06/18, $M = 7.8$). As in Tinnon *et al.* (1995), we use a seismogenic thickness of 20 km and the shear modulus is $\mu = 4.5 \times 10^{10}$ Pa. Haines & Holt method allows not only the computation of a Kostrov summation, but simultaneously solves for a spatially continuous modelled strain-rate field. To ensure an effective continuity of the strain-rate field for cells without any observed earthquake, an 'incompleteness' factor is introduced through the addition of a given level of isotropic variance in each cell. Non-zero modelled strain in cells where no deformation is observed is then allowed by continuity. In cells where we do observe seismicity, this added isotropic variance is equivalent to a larger error on the observed principal axes directions. In other words, this incompleteness factor allows continuity of the modelled strain-rate field, and it also allows observed and modelled principal axes directions to slightly differ in order to reach the best global fit. We use a level of isotropic variance equivalent to the one of Tinnon *et al.* (1995). We plot in Fig. 3 the observed and modelled strain-rate fields. Both fields are dominated by four large events: Cocos earthquake in the WB, two strike-slip earthquakes in the same cell along NyR and one large extensive earthquake near Chagos Laccadive. These earthquakes account for 79 per cent of the total seismic moment release in the oceanic domain for the last 100 yr. The associated velocity field is shown in Fig. 4 in an Indian reference frame. Australia rotates anticlockwise with respect to India, and NyR represents a real discontinuity for the direction and the amplitude of the velocity vectors. The velocity west of the NyR is negligible but increases east of the ridge.

Motion of Cocos GPS station with respect to India (Fig. 4) is only 3 mm yr^{-1} where GPS measurements indicate a 15 mm yr^{-1} velocity. The Kostrov velocity field is thus largely underestimated. The main reason of this underestimation is probably the fact that the
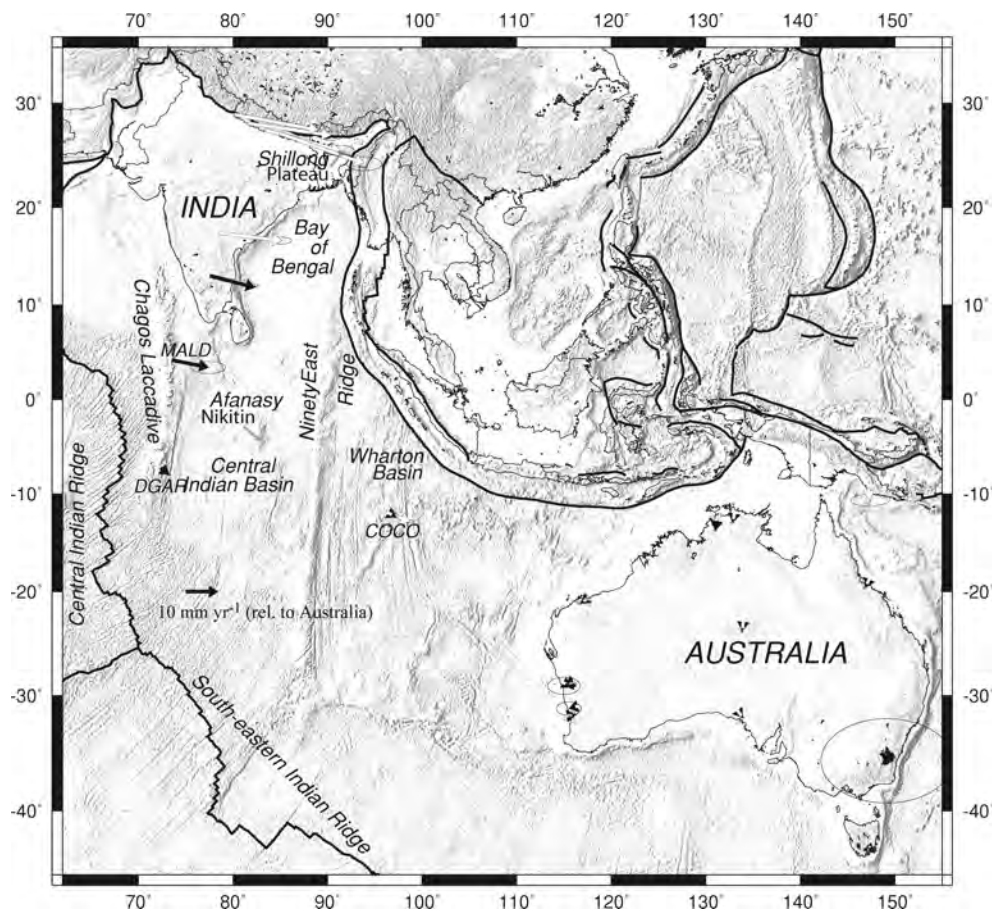
Figure 1. General overview of the Indo–Australian Plate. Socquet *et al.* (2006) (white) and Heflin *et al.* (2004) (black) GPS velocities are displayed in an Australian reference frame. Error ellipses are 1σ.

Table 4. GPS velocities from Paul *et al.* (2001) in mm yr^{-1}, Indian reference frame.

Stations	Latitude	Longitude	V_E	V_N	σ_{V_E}	σ_{V_N}
JNUC	28.54	77.17	0.80	−3.67	2.52	1.49
RANG	13.03	76.97	−0.13	−0.01	2.76	1.32
IISC	13.02	77.57	−1.47	−1.40	1.00	1.00
KRIS	12.95	78.52	−1.01	0.27	2.54	1.31
NANM	12.93	80.18	−0.18	−0.58	2.98	1.60
DEVA	12.63	77.63	−0.29	0.49	4.39	1.93
CHEN	11.16	77.59	0.89	1.12	2.60	1.49
MANA	10.66	78.46	1.07	−0.88	5.95	3.02
PLGT	10.83	76.82	3.35	−0.68	6.49	2.99
PLNI	10.43	77.56	6.42	1.19	8.38	4.47
MIJA	13.06	74.94	5.99	1.17	5.55	2.57
SHIL	25.53	91.85	0.88	−6.31	7.60	3.80
DELO	27.09	88.50	−2.46	−5.58	8.47	4.18

Bold station names are within our deformable grid.
Uncertainties are 1σ errors.

catalogue is not fully representative of the long-term deformation, a well-known limitation of the Kostrov method. Many of the historical earthquakes that occurred far from land are missing. In addition, spreading the energy of the biggest earthquakes in Haines & Holt method has severe drawback: it also smoothes the style of deformation around large earthquakes which is quite destructive. This impossibility to spread high amplitudes around one single event is the reason why our modelled velocities are not larger than that of

Tinnon *et al.* although we do include the supplementary Mw7.9 Cocos earthquake, the largest event by far in the region (33 per cent of the total seismic moment release in the oceanic domain).

Although the size of earthquakes may be difficult to use, their styles show great spatial coherency over a large spectrum of earthquakes amplitudes. To ensure that smaller earthquakes are indeed representative of the deformation style, we performed a Kostrov summation of the seismic moments for earthquakes with $M_0 < 10^{18}$ N m on an extended grid (Fig. 5). Since the majority of the earthquakes in our catalogue are scattered in this range of magnitude, there is no concentration of deformation near much larger events. The model shows a remarkably self-coherent strain-rate style for the entire Indian plate, indicating reliable focal mechanisms for all low magnitude earthquakes. The compressive axis rotates from NW to SE in the WB and along the NyR, where shearing occurs, to N–S shortening in the northern CIB and the Bay of Bengal (Weissel *et al.* 1980; Cloetingh & Wortel 1986). Rotation continues with the Shillong plateau where the compressive axis becomes NE–SW oriented. This rotation is rather continuous except between the NyR and the CIB where a quite brutal discontinuity appears. As expected from the location of the earthquakes, the Chagos Laccadive extension is concentrated in a tight zone.

3.2 Unconstrained geodetic model

Another way to compute the instantaneous strain-rate field is to spatially derive a geodetic velocity field obtained by fitting observed
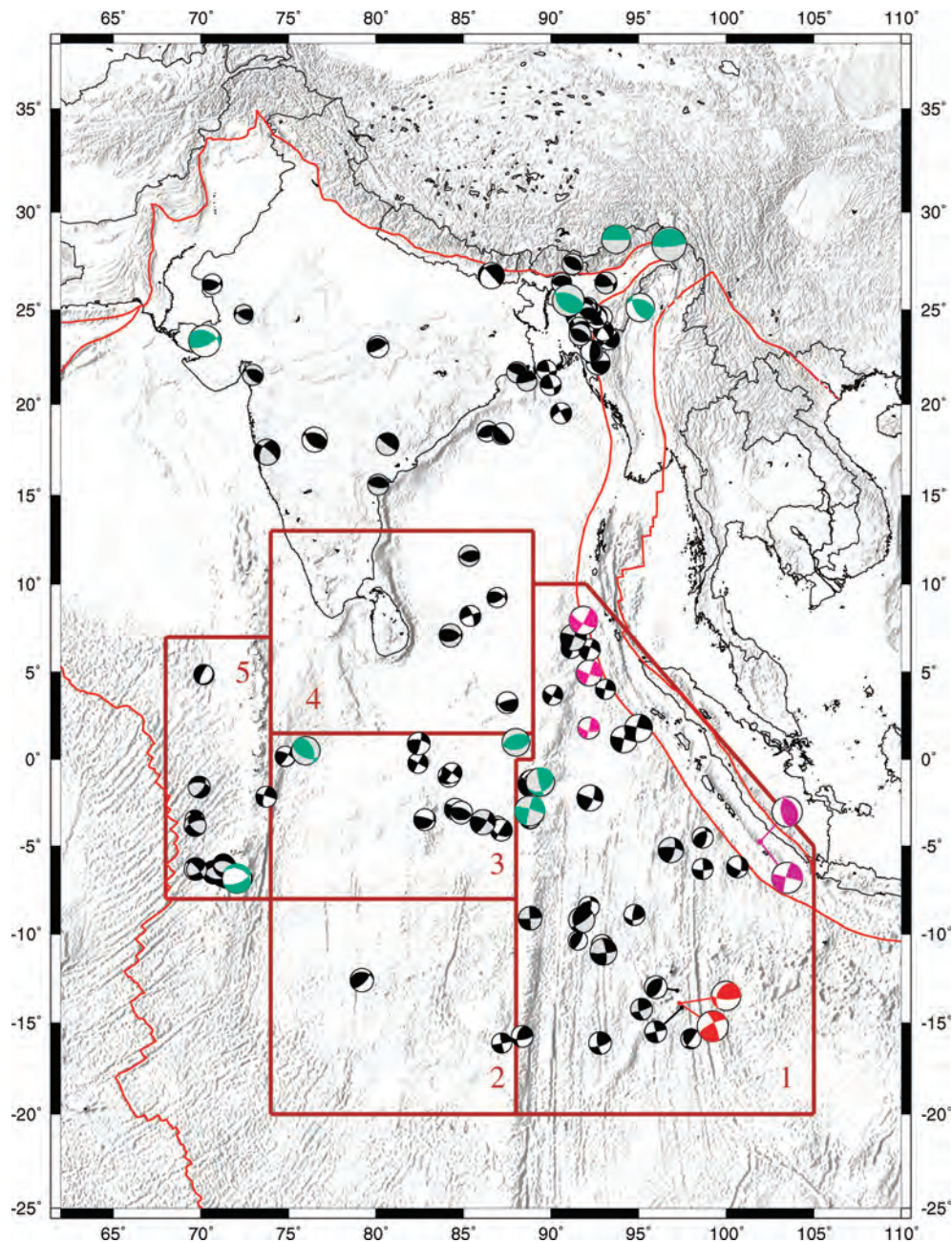
Figure 2. Intraplate seismicity. Red focal mechanisms are related to the 2000 June Cocos Island earthquake, pink ones are three aftershocks of the 2004/12/26 Aceh megathrust earthquake. Purple mechanisms are the two subevents of the 2000 June Enggano earthquake (not included in our study). Green mechanisms are other large earthquakes (*M* > 7). Grey mechanisms are pre-1976 events. Five subdomains discussed in the text are delimited. (1) WB, (2) Southern CIB, (3) Central CIB, (4) Northern CIB and (5) Chagos Laccadive.

GPS velocities in a least-square sense. The model is referred to as 'unconstrained' because no other constraints than GPS are used. Model velocities are spherically expanded in terms of a rotation vector function attached to each knotpoints of a grid using bi-cubic splines (a full discussion of the method is presented in Holt *et al.* (2000), Beavan & Haines (2001)). We now allow all cells from the Indian plate above 20°S to deform. We chose a rigid Australian reference frame. Rotations to bring each of the four GPS studies into a common Australian frame are solved simultaneously in the model. An output of the model is thus an ITRF2000/Australian pole for Socquet, Heflin *et al.* and Banerjee *et al.* data sets, and an India/Australia pole for Paul *et al.* data set. Deriving these poles is

quite straightforward for Socquet and Heflin *et al.* since both studies have stations located onto the Australian plate. It is more subtle for the solutions of Paul *et al.*'s (2001) and Banerjee *et al.* since the rotation is obtained from stations located only in India. Uncertainties associated with Socquet and Heflin *et al.* GPS velocities are formal errors and are thus very small. To avoid overfit, we scaled them so that the mean error in each set is larger than the mean residuals at Australian stations (~1 mm yr^{-1}). In this GPS-alone model, we use a uniform base level of strain rate variance for each grid cell. This uniform variance is in fact analogous to uniform strength or uniform rheology throughout the model (Haines & Holt 1993; Haines *et al.* 1998; Holt & Haines 1995).

Table 5. GPS velocities from Banerjee (2005) in mm yr^{-1}, ITRF2000 reference frame.

Stations	Latitude	Longitude	V_E	V_N	σ_{V_E}	σ_{V_N}
IISC	13.02	77.57	47.720	33.070	1.090	1.610
HYDE	17.42	78.55	45.920	34.250	1.080	1.430
NAGP	21.39	79.28	44.470	34.150	1.640	1.690
BHOP	23.21	77.38	43.140	33.190	1.580	1.650
JHAN	25.45	78.61	41.750	32.580	1.620	1.610
DHAN	23.82	86.44	51.040	32.840	3.130	2.890
LUCK	26.89	80.94	41.180	27.690	2.740	2.320
SHIL	25.53	91.85	50.080	28.890	2.860	2.130
DELH	28.48	77.13	47.710	32.810	2.770	2.640

Bold station names are within our deformable grid.
Uncertainties are 1σ errors.

The main drawback of the unconstrained model is that it is merely similar to a linear interpolation. The model favours pure shear rather than simple shear, so that the direction of compression is well reproduced but localized shearing is not. Fig. 6 shows the modelled strain-rate field. MALD and DGAR stations introduce a small but significant amount of extension. The southern motion of the SHIL station mainly induces a rotation of the compressive axis in the Bay of Bengal and Shillong plateau from NW–SE to N–S, which is more coherent with the orientation of the *P*-axis from seismicity. Finally, COCO station introduces a slight rotation of the compressive axis in the southern WB from NW–SE to a more eastward direction that fits well the observed compressive axis of the 2000 June Cocos Island earthquake (Locations of the COCO, MALD, DGAR stations and the Shillong Plateau are shown in Fig. 1). The amplitudes of the strain-rate field are linearly distributed from India to rigid Australia. This model approach is more adapted for dense GPS networks (Beavan & Haines 2001). Again, the spatial density of GPS measurements is too low to be conclusive, but to first order India appears at places relatively rigid compared to the oceanic domain. Three GPS stations measured by Banerjee (2005) constrain a rigid core in central continental India (strain-rates are less than 10^{-9} yr^{-1}). Cells where a non-negligible deformation occurs are due to conflicting GPS vectors on a short distance. Strain rates there do not reflect a coherent field (extension, strike-slip and compression in nearby cells in southern India and northern India). We definitely need more accurate data in these regions to know whether the rigid core extends south and north or not.

3.3 Anisotropic variance in kinematic modelling: combination of GPS and earthquake data

None of the two methods formerly described reaches a satisfactory strain-rate field. Kostrov summation of seismic moments produces a reliable strain style but amplitudes of deformation are unreliable and the associated velocity field is underestimated. On the other hand, the unconstrained GPS modelling does not catch the complexity of the strain-rate field mainly because of the poor spatial distribution of the stations. The two approaches are clearly complementary and the strength of Haines & Holt method is to allow the combination of both GPS and seismicity data. We thus performed a GPS inversion with constraints from earthquakes by introducing anisotropic variances in the model. Unlike isotropic variances, which equally authorize all directions of deformation in a cell, anisotropic
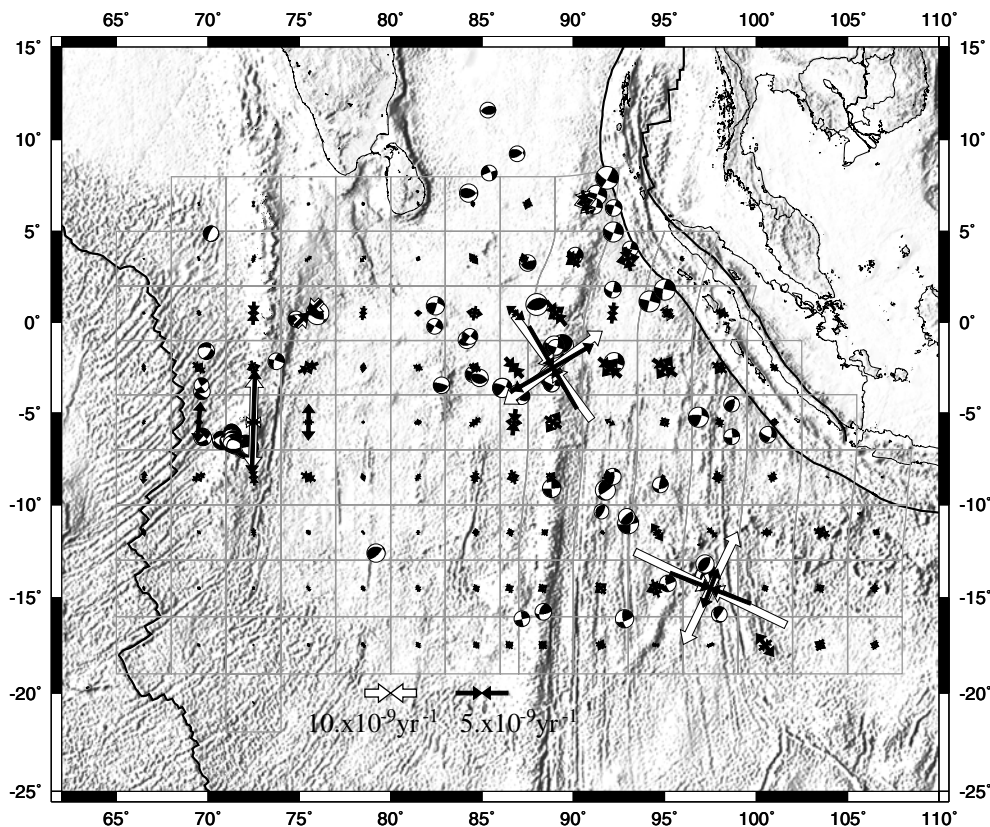
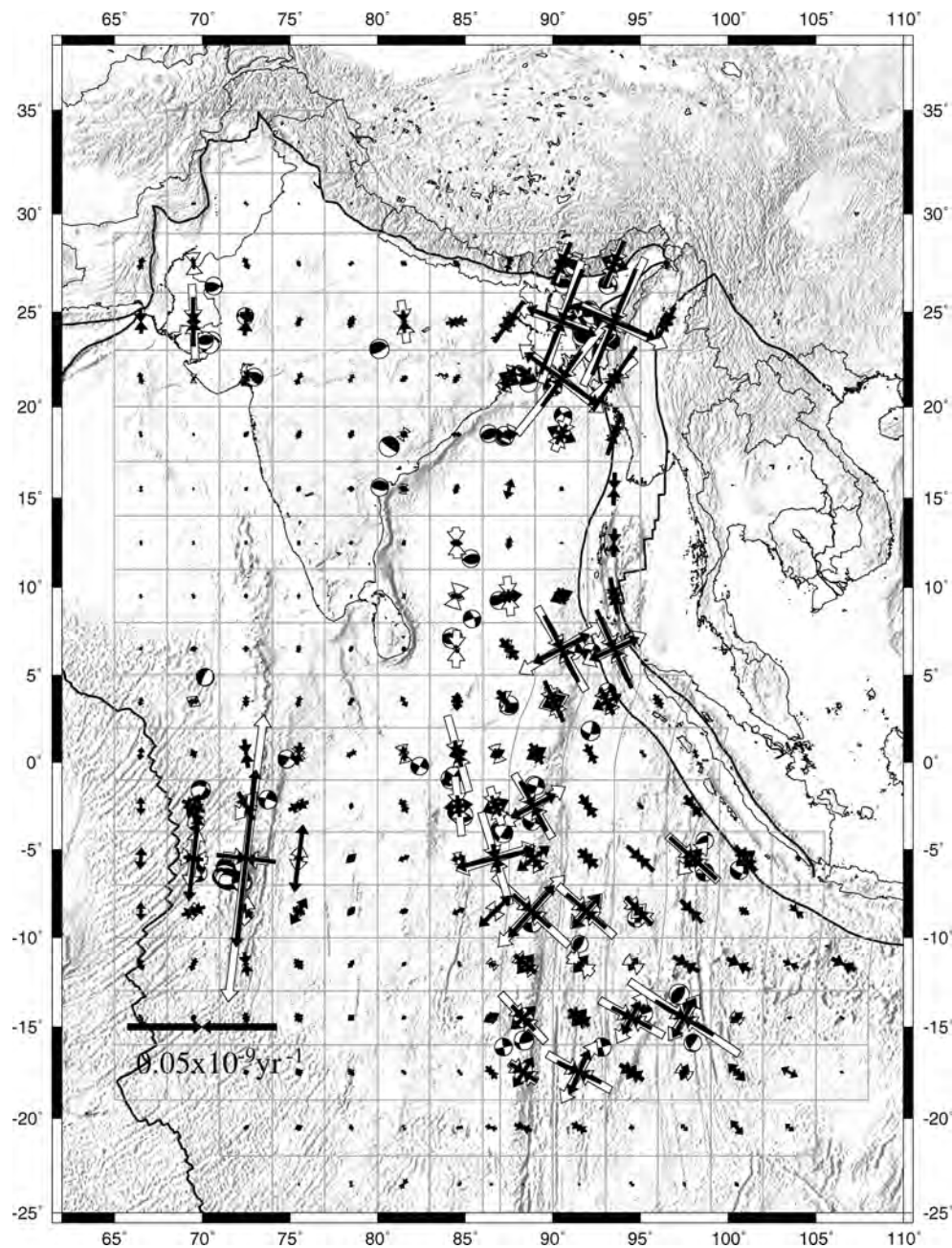**Figure 3.** Observed (white) and modelled (black) strain-rate fields inverted from Kostrov summation of seismic moments. Four large events in the Indian Ocean dominate the strain-rate field, occulting the background seismicity.
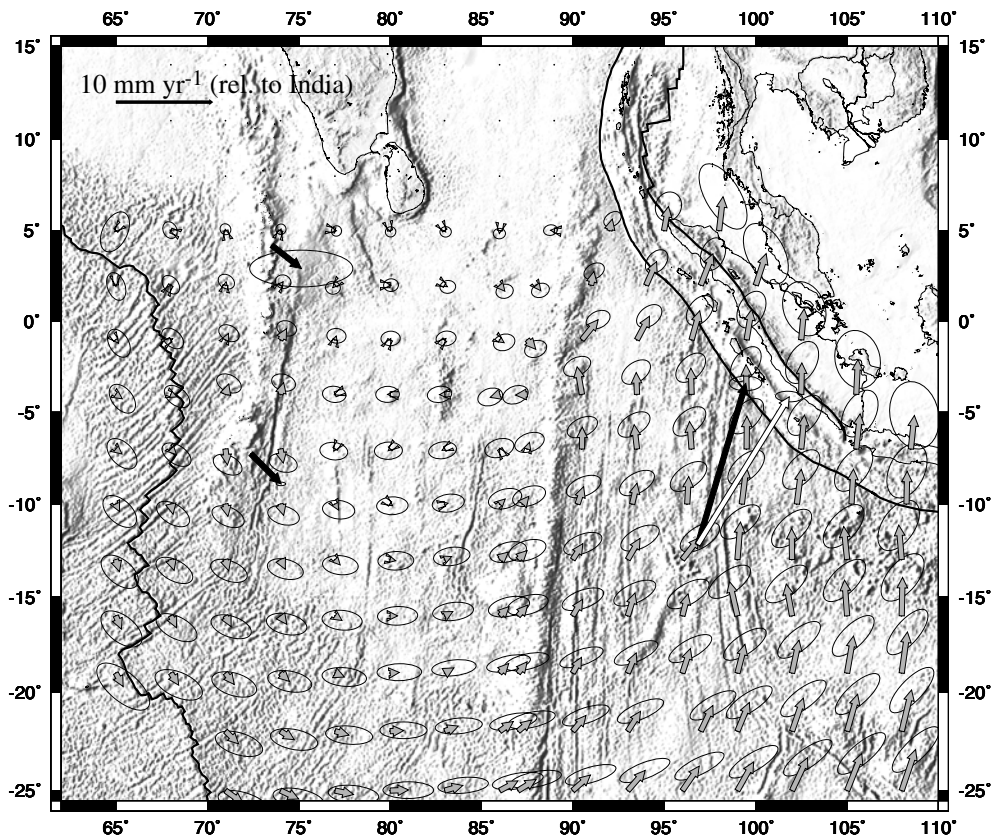
Figure 4. Velocity field inverted from Kostrov summation of seismic moments (Indian reference frame). The modelled velocity field is strongly underestimated when compared to the measured GPS velocities at station COCO, MALD and DGAR (white: Socquet (2003), black: Heflin *et al.* (2004.2)). Error ellipses are 1σ.

variances add constraints on the expected style of deformation (i.e. pure shortening or extension, strike slip or intermediate). The expected style of deformation is defined by the Kostrov method previously used. The anisotropic variance only defines the main direction of the principal axis of deformation, so that there is no *a priori* information between pure shortening and pure extension, or between sinistral and dextral strike-slip. Anisotropic variances contain no information about the relative levels of seismicity in cells. In other words, each cell has the same ability to deform, since at that point we still use a uniform base level of variance (equivalent to uniform rheology).

The modelled strain-rate field is shown in Fig. 7. The style of deformation is coherent with extension near Chagos Laccadive, sinistral shearing in the WB and along the northern NyR. The discontinuity between strike slip along NyR and shortening in the CIB and southern Bay of Bengal is quite well reproduced, the NyR acting as a boundary for contrasting styles. Seismicity of the Shillong plateau involves NE–SW shortening in the northeastern continental India and in the northern Bay of Bengal. We do not detect major incompatibility between the GPS far-field kinematic constraints and the main directions of deformation obtained by Kostrov summation of seismic moments. The fact that all regions have the same ability to deform still implies that the strain rate is linearly distributed between convergent India and Australia. The modelled strain-rate field is still close to the isotropic model field to first order although complexity has clearly been added to the style. The obtained strain rate amplitudes distribution somewhat contradicts with seismic profiling and seismicity distribution, since both data types point to localize deformation in narrower areas such as the northern NyR (i.e. the

part of the NyR that separates the CIB and WB between ∼10°N and ∼5°S) and the northeastern CIB (region 3 in Fig. 2). Localization is indeed obtained in the global model of Kreemer *et al.* (2003) based on the same Haines & Holt method. The reason for their better localization is that deformed and rigid regions are introduced *a priori* in their modelling. A noticeable difference is that our anisotropic model shows strike-slip in the subducting plate at the Sumatra trench, where the strain-rate field in Kreemer *et al.* is pure shortening and sometimes slightly 'implosive'. A major difference is that their model being global, all plate boundaries are included: the imposed continuity of the strain-rate field across the Sumatra subduction zone can only be reached by distributing deformation on both sides of the trench. Using small size and highly deformable grid cells at the trench may be a good way to absorb convergence over a short range. The difficulty in the case of the Sumatra trench is that intraplate deformation persists close to it, and possibly within the upper portion of the slab engaged into the subduction. The proper way to derive the internal velocity is thus to solve for the intraplate field only.

4 STRAIN-RATE FIELD IN AN ANISOTROPIC AND NON-UNIFORM MEDIUM

4.1 Non-uniform model from seafloor ages

A further step towards complexity is to introduce weaker zones (Tinnon *et al.* 1995) through the use of non-uniform and anisotropic variances. In addition to the expected deformation style, we

Figure 5. Observed (white) and modelled (black) strain-rate fields inverted from Kostrov summation of seismic moments with $M_0 < 10^{18}$ N m. These 91 earthquakes show great internal consistency, and are thus representative of the deformation style.

assigned a larger level of variance to grid cells considered to be in weak zones, thus allowing these to deform faster than others. In the oceanic domain, the rigidity of the lithosphere is expected to increase with the age of the seafloor (Watts *et al.* 1980). We use as before the anisotropic variance obtained from Kostrov summation of seismic moments, but scale them with a rheological factor. The scaling factor is chosen inversely proportional to the age of the oceanic lithosphere from Muller *et al.* (1997). For continental India, we chose to introduce a level of variance equivalent to the one used for the oldest oceanic lithosphere based on the recent estimation of a strong India lithosphere (Hetényi *et al.* 2006). As expected, the obtained strain-rate field (Fig. 8) concentrates in the

WB, because of the younger ages near the fossil Wharton spreading ridge compared to the age of seafloor at similar latitude west of the NyR. Deformation is also high in the south of the CIB, but not near the Central Indian Ridge. The reason is that Diego Garcia GPS velocity is very small relative to our rigid Australia, so that deformation is small irrespective to the age of the lithosphere. The same is true southeast of Cocos Island, where GPS velocity is nearly Australian. The northern part of the CIB and the Bay of Bengal do not deform significantly since their lithosphere is rather old (∼80–90 Ma). Deformation is probably underestimated there, since we do observe seismicity and active faulting in the northeastern CIB.
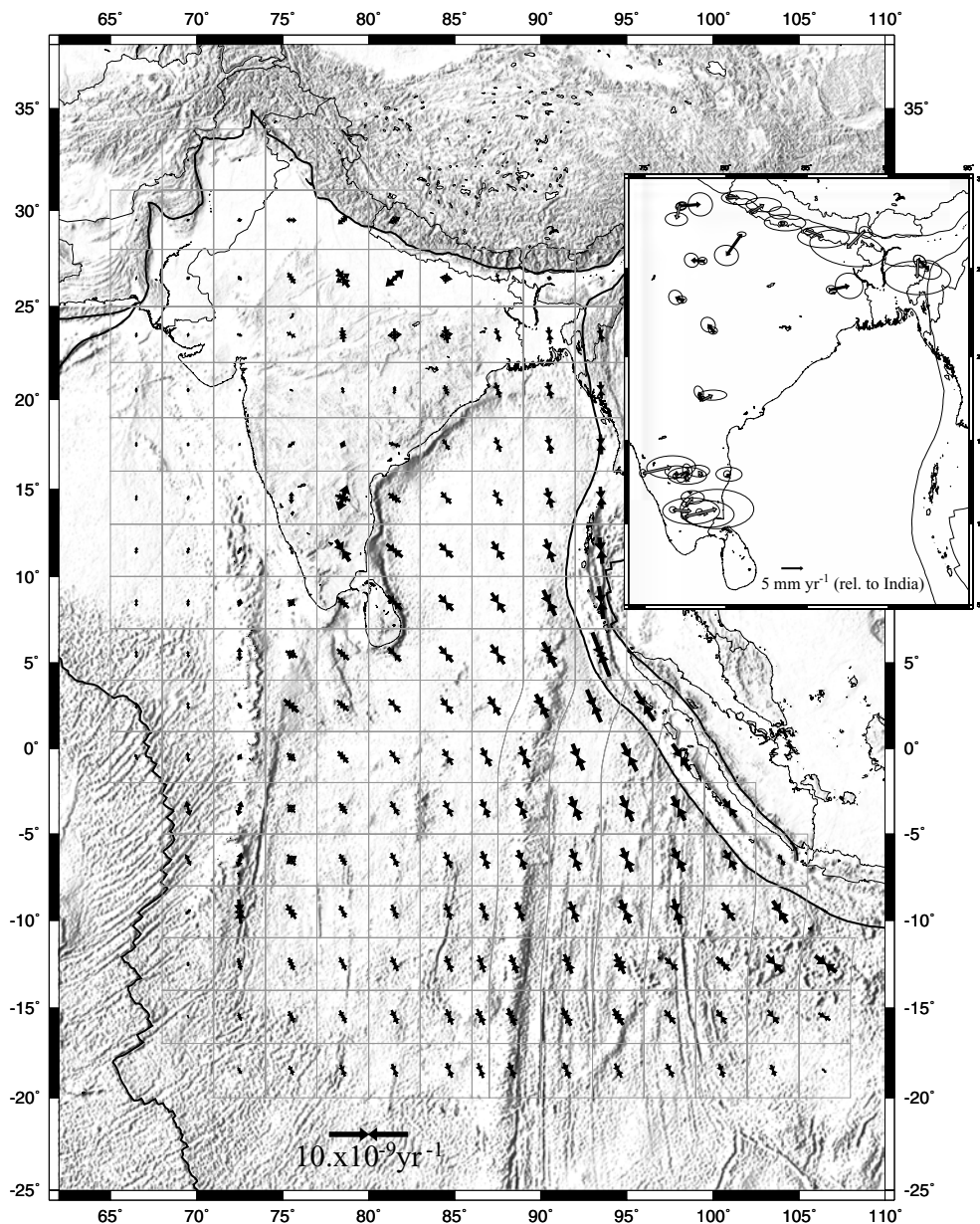
Figure 6. Modelled strain-rate field obtained from unconstrained GPS modelling, residuals of Indian GPS velocities are also shown.

4.2 Heat flow as an indication of localized lithospheric weakness

This age related model does not take into account some possible localization effects due to pre-existing structures and/or hotspot intraplate volcanism (Royer *et al.* 1991). A different approach is to scale the level of variance with surface heat-flow, which is a combined measure of thermal anomalies and plate cooling with age. We use the global heat-flow compilation of Pollack *et al.* (1993) that contains more than 300 heat-flow values in the considered oceanic region. We first interpolate the data with a Kriging algorithm and then compute the average heat flow in each cell of the grid (Fig. 9). High heat flow values are then converted to large scaling factors, that is, large weakness. Heat-flow is high near the Afanasy Nikitin seamount (above $100 \, \text{mW m}^{-2}$) (Weissel *et al.* 1980), higher than the $55 \, \text{mW m}^{-2}$ heat-flow expected for a ~80–73 Ma old lithosphere

(Krishna 2003). Although the measurements often come from old surveys and, therefore, may not be accurate, we believe that ~10 values above $80 \, \text{mW m}^{-2}$ obtained from different studies are reliable enough to show evidence for a large thermal anomaly in the region (we rejected for our interpolation heat-flow measurements greater than $200 \, \text{mW m}^{-2}$, to avoid too high discontinuities maybe due to strong fluid circulations). Moreover, a complete heat flow profile with more than 40 measurements has been acquired for the ODP Leg 116 (Cochran *et al.* 1989) and the average heat flow is $84 \, \text{mW m}^2$, that is to say a ~$30 \, \text{mW m}^2$ anomaly. The origin of the high heat flow anomaly remains speculative (Geller *et al.* 1983; Stein & Weissel 1990). Fluid driven flow is unlikely to explain the anomaly alone (Weissel *et al.* 1980): sea water fluid circulation would drop broadly the heat flow (distributed input) and increase it punctually (localized output). This is what we see along the Indian spreading ridges, where high heat-flow values are located amongst very low background
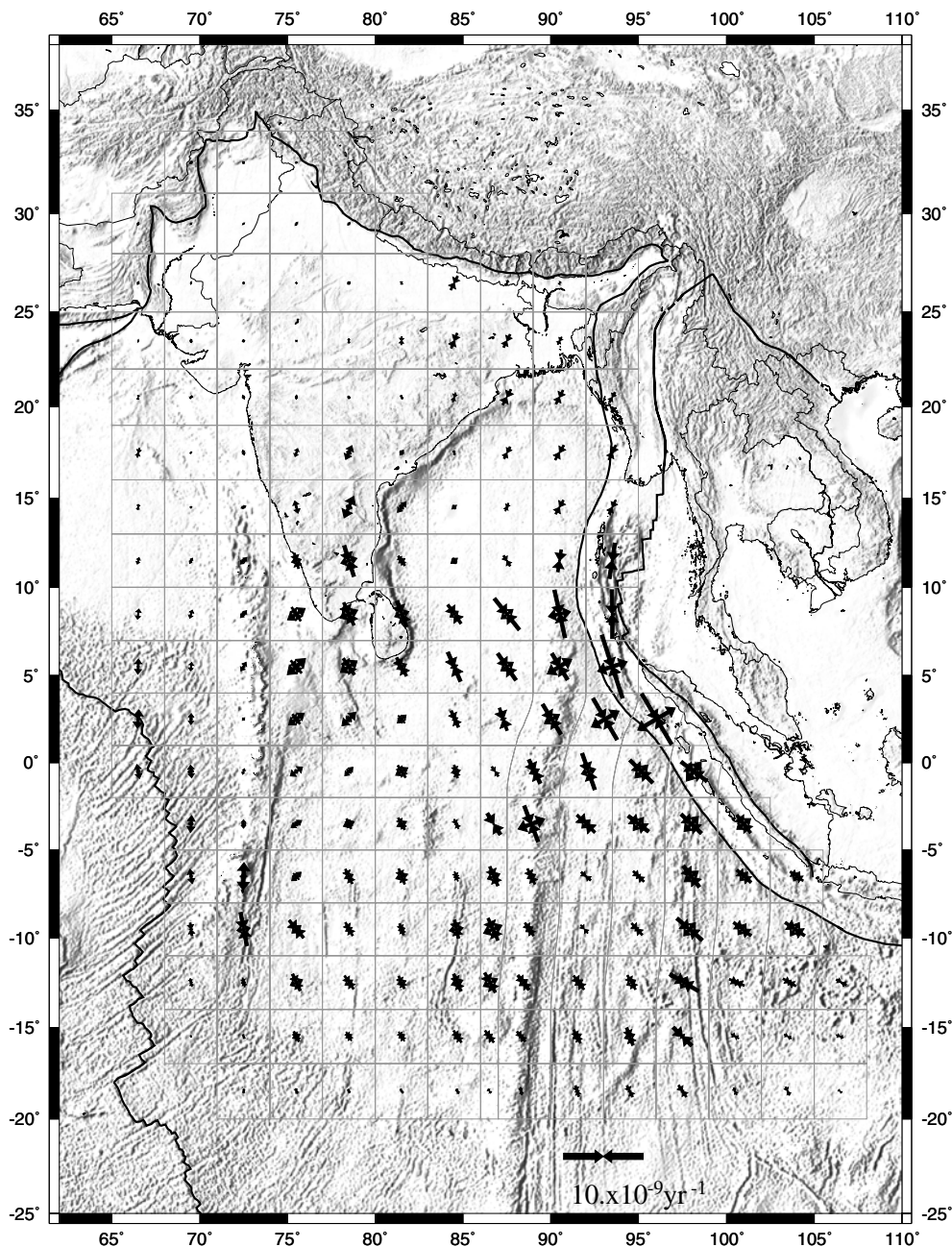
Figure 7. Modelled strain-rate field obtained from GPS modelling with anisotropic variance. Deformation is favoured in the direction of principal axis of deformation obtained from Kostrov summation. See discussion in text.

values. The exact opposite is found in the vicinity of Afanasy Nikitin (Geller *et al.* 1983). Two other mechanisms have been proposed to explain the high thermal anomaly. Hotspot volcanism could have reheated the base of the lithosphere and increase surface heat-flow several million years later through conduction. Indeed, the ANS was emplaced on a low elastic thickness lithosphere near a spreading ridge crest (Karner & Weissel 1990; Paul *et al.* 1990) and was probably reactivated 35 Ma later (Krishna 2003). However, reheating is rejected by Stein & Weissel (1990) who pointed out that no large-scale bathymetric swell is observed: the bathymetry seems normal for the age of the lithosphere. Another possibility is that the heat-flow anomaly results from the deformation itself as an effect of friction on the inverse faults network in the CIB. Faulted zone from Phèdre seismic profiles (Jestin 1994) exactly corresponds to

the high heat flow area. Despite the high number of faults, the mean strain rate is small and it is unlikely that friction can contribute significantly to the observed high heat flow (Geller *et al.* 1983). Our first order calculation (using Lachenbruch & Sass 1980, 1992; Carslaw & Jaeger 1959, modified for thrust faults) indicates that the maximum contribution does not exceed 5 mW m^{-2}. It has also been proposed that widespread exothermic serpentinization in the CIB may be a cause of the anomalous surface heat flow (Verzhbitsky & Lobkovsky 1993; Delescluse & Chamot-Rooke 2006).

Although the origin of the thermal anomaly remains debatable, our heat-flow based model (i.e. a weak Afanasy Nikitin) well reproduces the observed strain (Fig. 10). As expected, the deformation now localizes in the northern CIB, with a strong N–S compressive component, in contrast with sinistral strike-slip along the NyR and
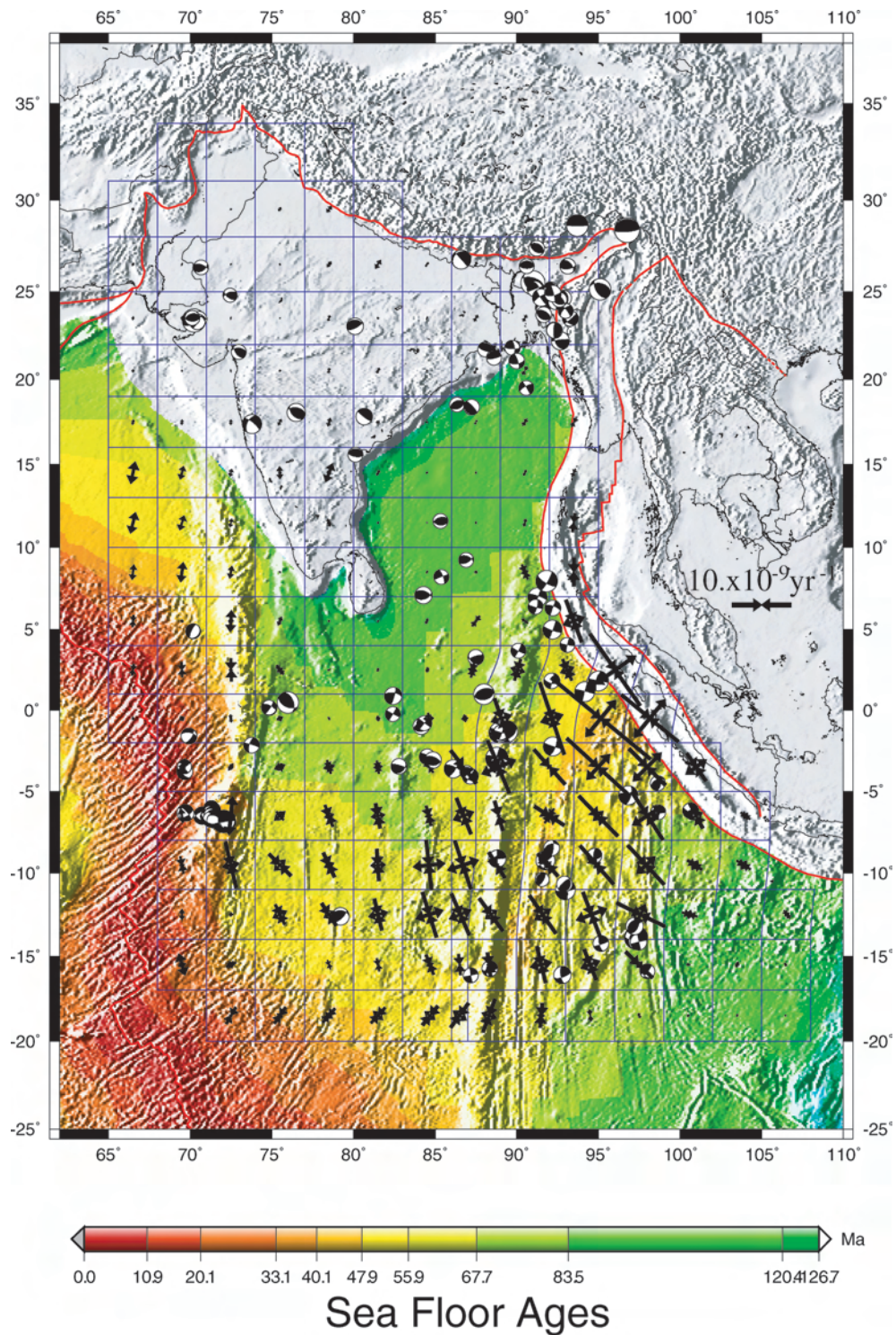
Figure 8. Modelled strain-rate field obtained with non-uniform variances scaled with seafloor ages. The base level of variance is attributed to continental India, then a scale factor inversely proportional to the age of the oceanic lithosphere is applied.

in the WB. Note that the deformation also localizes north of the NyR although there seems to be no thermal anomaly there: the contrast between the styles of deformation alone allows localization. High strain rates also prevail in the WB, as in the previous homogeneous models. This would suggest that in the model, high strain there is required by seismic and GPS constraints. Moderate extension also appears near Chagos Laccadive.

5 DISCUSSION

5.1 Models comparison

The introduction of anisotropic variances is an obvious ameliora-tion of the uniform-isotropic model which cannot pretend to fit the observations very well, particularly not the style of deformation.
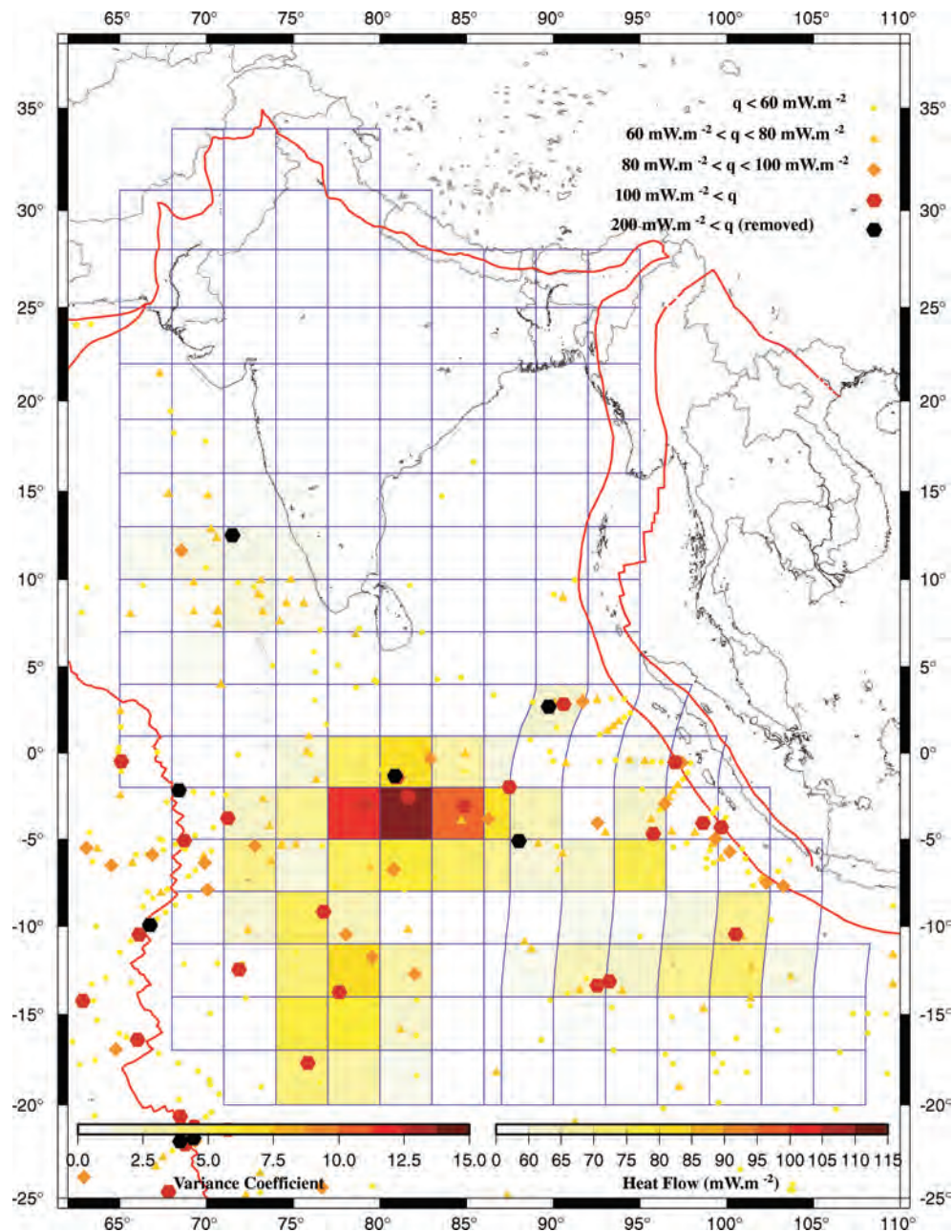
Figure 9. Inferred weak zones from heat flow. Heat flow is interpolated by kriging, and then averaged in each cell; values are used to determine a scale factor applied to the variance.

However, at this point, we cannot clearly determine which of the three anisotropic models (homogeneous, heterogeneous as a function of age, heterogeneous as a function of surface heat flow) can objectively be regarded as 'best'. We are thus forced to cross-check several types of comparisons between observations and models.

All models equally well fit the GPS velocities with a weighted residual of approximatively 1 mm yr^{-1}. Indeed, this is the localization of deformation between India and Australia that changes between our different anisotropic models and not the fit to the GPS velocities, especially as virtually no GPS stations are in the oceanic deformation zone. Modelled strain-rate amplitudes cannot be directly compared to strain rates obtained from Kostrov summation of seismic moments since the earthquake catalogue does not well represent the long-term spatial release of strain. We are left with

two other types of comparisons: (1) modelled versus observed relative moment rate release between regions and (2) degree of fit of the modelled principal axis directions of strain-rate to the observed directions.

5.1.1 Predicted moment rates versus observed moment rate from historical seismicity.

In Fig. 2, we divided the Indo-Australian plate into five subdomains based on their characteristic styles of deformation: the WB, the southern CIB, the central CIB, the northern CIB and the Chagos Laccadive Ridge region (respectively, regions 1, 2, 3, 4 and 5). The first row of Table 6 gives the observed moment rate from historical seismicity in each of these regions. The second row displays their
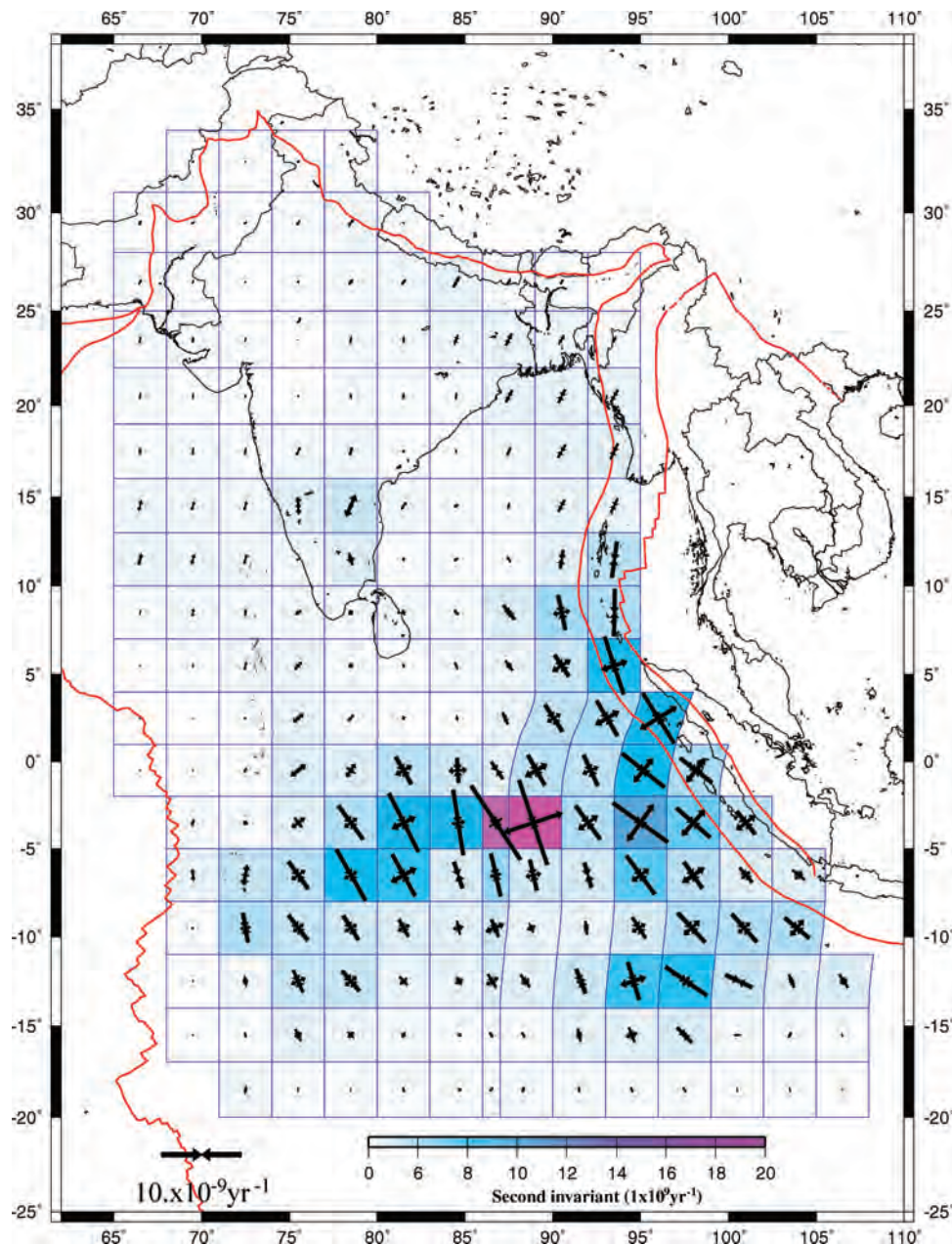
Figure 10. Modelled strain-rate field obtained from our preferred model. The base level of variance is attributed to continental India and to cells where average heat flow is below 55 mW m^{-2}. Elsewhere, variances scaling factors are derived from the surface heat flow (Fig. 9).

equivalent ratios to region 1. The WB is the only region where the predicted moment rate is quite stable for our four models, so that we use it as the reference (see Table 6 for the details of the fault geometry used to compute moment rates from modelled strain rates). WB moment rate is 1.76–2.98 times the observed moment rate, confirming that the catalogue is not complete or inaccurate. If we consider only the last 25 yr of instrumental seismicity, the ratio of observed to modelled falls closer to 1 (0.83) owing to the Mw7.9 Cocos earthquake (2000 June) that dominates the moment release. In our opinion, the gap between observed and predicted moment rate can easily be filled by some unreported and/or misreported similarly large historical earthquakes.

The four remaining rows in Table 2 display for each region the ratio to the moment rate in the WB for the considered model. We can now compare these ratios to the observed ratios. Notice that there is nearly no observed deformation in region 2 and 4. Two thirds of the total observed moment rate is released in the WB, one-sixth in region 3 (26 per cent of WB) and the remaining one sixth in region 5 (28 per cent of WB). Absence of deformation in regions 2 and 4 cannot be obtained in any of our models because of the necessity to have a continuous field. However, only the anisotropic, non-uniform heat flow model concentrates enough deformation in region 3 (39 per cent of WB predicted moment rate) with relatively low deformation in regions 2 and 4 (16 and 11 per cent of WB moment rate). The anisotropic-uniform model releases a too high moment rate in region 4 and a too low moment rate in region 3 (41 and 17 per cent of WB moment release). The anisotropic model with non-uniform variances from seafloor ages implies a too high

Table 6. Comparisons between observed moment release (from histrical seismicity) and predicted moment release (from our four different models) for five oceanic regions.

	1 (WB)	2 (South CIB)	3 (central CIB)	4 (north CIB)	5 (Chagos)
Observed moment rate	1.51×10^{19}	1.07×10^{16}	3.94×10^{18}	1.21×10^{16}	4.23×10^{18}
Nm yr^{-1} (ratio to WB)	(1.00)	(0.00)	(0.26)	(0.00)	(0.28)
Non-uniform—heat flow	1 (2.31)	0.16	0.41	0.11	0.06
Non-uniform—age	1 (2.98)	0.28	0.12	0.06	0.12
Uniform—anisotropic	1 (1.89)	0.20	0.17	0.41	0.12
Uniform—isotropic	1 (1.76)	0.24	0.19	0.34	0.11

This table compares the observed moment rates with the predicted moment rates in each of our four models for five regions displayed in Fig. 2. The five regions are, respectively, the Wharton Basin (WB), the southern Central Indian Basin (CIB), the central CIB, the northern CIB and Chagos Laccadive. Predicted moment rates have been computed for 45° dipping fault planes striking at 90° of the major principal strain rate axis direction. It also works for vertical strike slip faults oriented at 45° to both directions of principal axis. $\dot{M}_0 = 2\mu V(|\frac{1}{2}(\dot{\epsilon}_{\phi\phi} + \dot{\epsilon}_{\theta\theta})|) + \sqrt{\frac{1}{4}(\dot{\epsilon}_{\phi\phi} - \dot{\epsilon}_{\theta\theta})^2 + \dot{\epsilon}_{\theta\phi}^2}$ (Holt *et al.* 1995; Savage & Simpson 1997; Pancha *et al.* 2006) is thus the minimum moment rate computed in each cell of the grid (an angle different from 45° would imply a greater moment rate). This estimation is correct for the WB area where a NW–SE principal axis is accommodated by N–S strike-slip faults, but it is a minimum for the CIB since the principal axis direction slightly differs from N–S whereas faults remain mainly E–W. This underestimation does not exceed 20 per cent. We choose to present the results with respect to the moment rate in region 1 (WB) which gives quite stable results throughout our models. It is also the highest straining region. This allows comparison between regions, which is the criterion that has the lowest dependance on uncertainties such as the earthquake catalogue completeness or the parameters used for the predicted moment rate calculation (i.e. seismogenic thickness = 20 km, shear modulus = 4.5×10^{10} Pa). Bracketed values are ratios to the observed moment rate in the WB, other values are ratios to the predicted WB moment rate in the considered model.

Table 7. Goodness of fit of modelled directions of principal axis to observed directions of principal axis from seismicity.

Model	rms^a	rms^b	rms^c
Isotropic	23.7°	29.0°	26.5°
Anisotropic	16.5°	16.7°	19.9°
Non-uniform—age	19.0°	19.2°	21.3°
Non-uniform—heat flow	15.7°	19.7°	20.9°

[a]Residuals are weighted with the modelled second invariant of strain-rate.
[b]Residuals are weighted with the number of earthquakes in each box.
[c]Non-weighted residuals.

moment rate in region 2 (28 per cent of WB moment rate) where seafloor is young, and there is not enough deformation in region 3 in this 'age model' (12 per cent of WB moment rate instead of 26 per cent).

5.1.2 Goodness of fit of modelled strain-rate axis to observed strain-rate axis from seismicity

We must now ensure that the best relative repartition of deformation is not obtained at the expense of the fit to the observed style of deformation. In Table 7, we analyse the goodness of fit of the modelled strain-rate axis direction to the observed strain-rate axis direction from seismicity. Non-weighted rms confirm that the introduction of anisotropic variance greatly improves the models, with a much larger rms value for the isotropic model (26.5°) than for the other models (∼20°). In the remaining columns of Table 7, weighted rms take into account the fact that we should give more credits to the fit where deformation is best catched by seismicity, that is to say where deformation is important. The first column shows the rms weighted by the second invariant of the modelled strain rate, and in this case, the 'heat flow model' has the best rms value (15.7°). The second column shows the rms weighted by the number of earthquakes in the cell. Here the anisotropic-uniform model clearly best fits the style (16.7°) but the two non-uniform models (19.2° for the 'age model' and 19.7° for the 'heat flow' model) still fit much better than the

isotropic model (29°). Weighting with the number of earthquakes may be less reliable since many of the medium size earthquakes may be absent from the focal mechanisms catalogue.

Globally, we see that the 'heat flow model' mainly localizes deformation where seismicity is significant, unlike all other models, and the fit to the observed style of deformation is either better, or almost as good as the anisotropic uniform model, depending on the weighting method. Using both types of criteria (distribution of deformation and fit of the style) we conclude that anistropic, non-uniform heat flow model is the best model we have in hand. Some interesting qualitative informations can also be extracted from this best model, as well as some more quantitative comparisons with finite deformation. This is what is now discussed in the next sections.

5.2 Localization of deformation in the CIB and along the northern NyR

5.2.1 NinetyEast ridge and Wharton Basin

Our preferred model actually confirms most of the inferences made by mechanical models (Cloetingh & Wortel 1985, 1986; Coblenz *et al.* 1998). Cloetingh & Wortel (1986) compute the state of stress in the whole Indo–Australian Plate (considered as a thin elastic layer) using boundary forces assumptions. The model predicts rotation of the principal axis of stress from NW–SE in the WB to a roughly N–S direction in the Bay of Bengal. Concentration of stress (several kilobars) occurs around the northern NyR in the same way that strain concentrates in both our homogeneous and heterogeneous models. However, Cloetingh & Wortel (1986) found no discontinuity in the rotation of principal stress axis across the NyR while our modelling suggests that NyR acts as a boundary for strain orientation and deformation style. This strain discontinuity (observed and modelled) along with the continuity of stress orientation across the ridge (Bergman & Solomon 1985) probably denote a weak rheology for the NyR, as inferred in Tinnon *et al.* (1995) and Deplus *et al.* (1998).

East of the NyR, in the WB, our modelled strain-rate field shows rather high diffuse left-lateral strike-slip deformation north of ∼5°S, in accordance with numerous focal mechanisms in the area

between the Sumatra Trench and the northern NyR. The deformation extends further south until ~15°S with a more eastward oriented compressional axis, fitting the style of seismicity near Cocos Island better.

5.2.2 Central Indian Basin

In the CIB, our preferred model shows, as for the NyR, high amplitudes of deformation around ~5°S, at the latitude of the Afanasy Nikitin seamount chain. Fig. 10 indicates a maximum of the second invariant of deformation between the ANS and the NyR, a location corresponding to a cluster of earthquakes, including magnitudes up to 7. Pure N–S shortening around Afanasy Nikitin is confirmed by both seismicity and seismic profiles. The weak ANS chain thus acts as a quite narrow equatorial kinematic barrier, resulting in a concentration of N–S shortening between ~0° and ~7°S.

This area also reveals a high level of finite deformation. The thrust fault network imaged by seismic profiles, dense below the equator, nearly disappears north of it (Van Orman *et al.* 1995; Jestin 1994; Chamot-Rooke *et al.* 1993) from the Central Indian Ridge to ~82°E. Immediately east of this longitude, one seismic line at 84.5°E from Phèdre Cruise (Jestin 1994; Chamot-Rooke *et al.* 1993) shows numerous thrust faults north of the equator. An additional seismic profile at 87°E from Krishna *et al.* (2001) also reveals deformation, but less severe than south of the equator. Krishna *et al.* (2001) proposed that multiphase folding of the oceanic lithosphere occurred since the onset of deformation 7.5–8 Ma ago (Cochran 1990). Detecting which of the three major unconformities (Miocene, Pliocene and Pleistocene) of the Bengal Fan sedimentation are cut by faults, they determine three areas, each corresponding to an episode of deformation. They show that the Miocene episode occurred south of the equator whereas the Pliocene one occurred north of it, while the Pleistocene episode is superimposed on the first two others in a roughly subequatorial zone. The vicinity of the Afanasy Nikitin seamount chain is thus the only area where all three episodes have occurred. This would suggest a continuum of deformation around Afanasy Nikitin since the initiation of deformation. Karner & Weissel (1990) also note that the Afanasy Nikitin seamount chain lies in the area where the deformation is best developed. They suggest that an initial deflection inherited from the Afanasy Nikitin seamount load favoured growth of large-scale buckling wavelength when compression started.

5.2.3 Rigid continental India and deforming Bengal Bay

In our preferred model, little deformation is predicted for continental India and the Bay of Bengal. Rigid India extends in the oceanic domain down to the NyR to the east (i.e. it includes the Bay of Bengal) and down to the equator to the south. Actually, since we do not have enough heat-flow data in the central Bay of Bengal, our weakening criterion may not be realistic there. Although a few measurements show a normal heat flow corresponding to the cooling of a cretaceous oceanic lithosphere, the relative rigidity of the Bay of Bengal lithosphere with respect to the Central Indian Ocean lithosphere may not be accurate in the model. The same is true for continental India, as we chose to attribute the lowest level of variance there (i.e. the equivalent of a cretaceous oceanic lithosphere, $q < 55$ mW m^2). The drawback is that since we do not force any localization of deformation at the feet of the Shillong Plateau, the southward motion of the plateau with respect to India is underestimated. However, the introduction of this underestimated southward motion in

the model is crucial in controlling the direction of the *P*-axes in the Bay of Bengal. The only robust result about continental India is the rigid core we discussed for the isotropic and homogeneous model, which remains whatever the choices made in all models. The fact that the anisotropic models show less deformation of continental India when compared to the isotropic-uniform model means that principal axis directions from sparse continental seismicity contradicts GPS residuals, forcing the code to minimize deformation. It confirms the poor accuracy of Indian GPS measurements with large residuals and error ellipses. Long-term GPS surveys are still needed to draw a definitive conclusion in the southern peninsula, near the Himalayan front and across the Shillong plateau.

5.2.4 Capricorn Plate

Notice that in our models, we defined only one Australian rigid plate whereas Royer & Gordon (1997) introduced an additional Capricorn plate between Chagos Laccadive and the ridges, allowing a better plate-circuit closure. We unfortunately do not have enough resolution to implement it, because there is of course no GPS stations and only a few low magnitude earthquakes. Kreemer *et al.* (2003), who did introduce the Capricorn plate, modelled a much more significant extension near Chagos Laccadive and also more deformation in the southwest WB. Hence, smaller deformation in our best model may be caused by the lack of a Capricorn plate. We could have 'forced in' Capricorn plate motion, but the rationale in this study was to avoid any kind of plate motion forcing or plate boundary interaction. We conclude from our modelling that the instantaneous motion of the Capricorn plate with respect to the other plates is below the resolution of the data we have in hand.

5.3 Finite versus instantaneous deformation

The velocity field is shown in Fig. 12. An India/Australia rigid pole of rotation was obtained by minimizing the modelled velocities at continental Indian GPS stations (Fig. 11). This pole, located at 11.3° S, 72.8°E (Table 10) describes the instantaneous intraplate kinematics and can be compared with those obtained from magnetic anomalies over larger timescales including Nuvel1A (DeMets *et al.* 1990, 1994a), DeMets *et al.* (1994b) and the more recent DeMets *et al.* (2005). Our short-term data and models seem to locate the pole slightly to the southwest of the finite poles (Fig. 11). The rotation rate of our pole ($-0.301°$/Ma) is of the same order than finite rotations. We also included two instantaneous poles from Kreemer *et al.* (2003) and Socquet (2003). Both are situated significantly northward from our pole (~5°) but their rotation rates are 33 per cent larger, resulting in similar predictions for Indian velocities. Instantaneous poles seem to describe a larger motion than finite poles, and we cannot totally rule-out a southward migration of the pole through time (or a rotation rate acceleration). However, all poles are indiscernible at the 95 per cent level of confidence, and as Kreemer *et al.* (2003) already pointed out, finite and instantaneous motions seem similar. To confirm this more quantitatively, we use two different ways to extrapolate finite displacements from instantaneous motion.

The first one is a classical baseline shortening computation using our IN/AU pole of rotation, and considering that extremities of all baselines are situated on rigid plates (Fig. 11, Table 9). We calculated several baselines length changes, in the WB, the CIB and Chagos Laccadive, including three that exactly overlap with the ones of Royer & Gordon (1997) (Table 9: B1, B2 and B3; short-
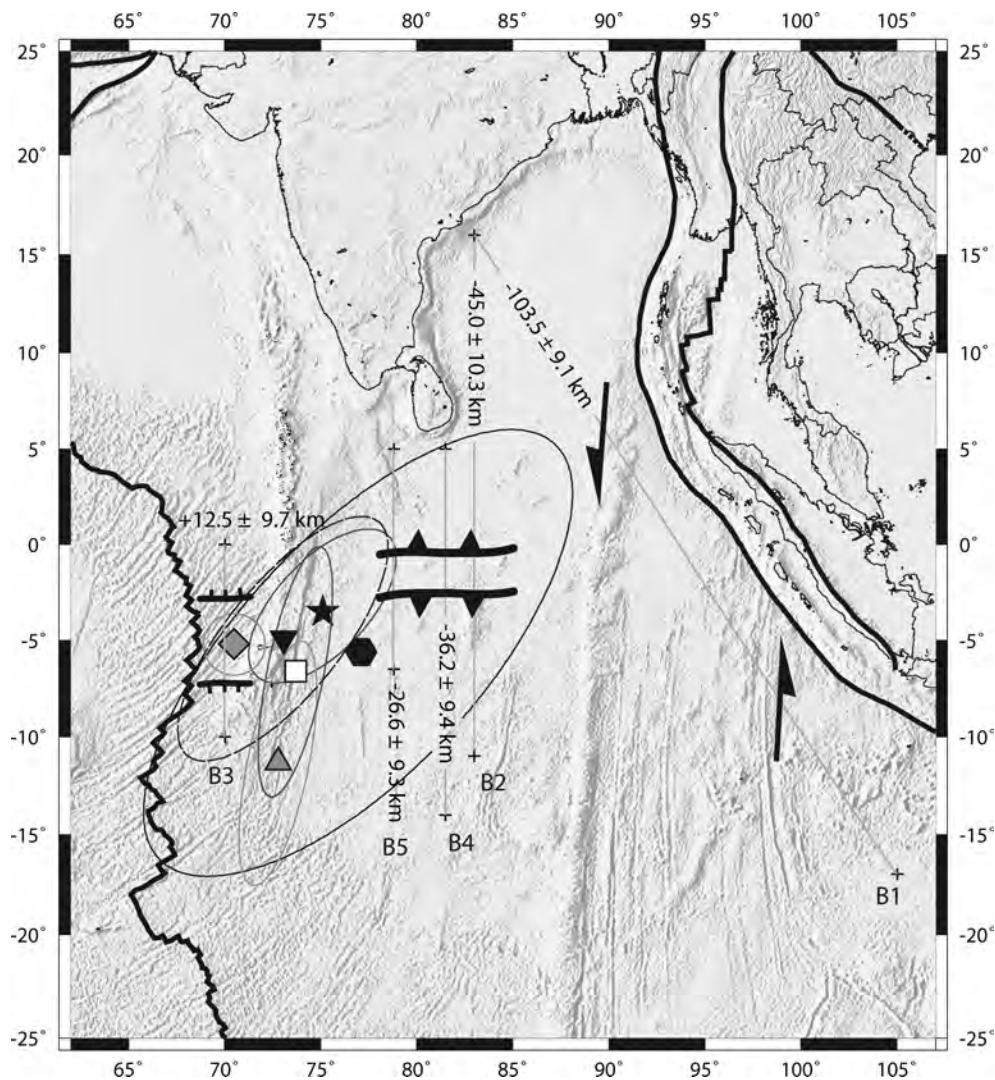
Figure 11. India/Australia rotation poles (Table 9) and baselines (Table 9). Ellipses and uncertainties are 2σ errors. Star: DeMets *et al.* (1994b). Hexagon: Nuvel 1A (DeMets *et al.* 1990, 1994a). Diamond: Kreemer *et al.* (2003). White square: Socquet (2003). Triangle: This study − GPS + earthquakes. Reversed triangle: DeMets *et al.* (2005) (India/Capricorn pole at anomaly 4n.2, 7.86 Ma). From east to west: baselines B1, B2,B4, B5 and B3 (Table 9).

ening obtained from plate reconstructions) and two others coincide with seismic profiles (Table 9: B4, B5; shortening obtained from PHEDRE multichannel seismic line and Conrad single channel seismic line). Our total amount of shortening is obtained by using the instantaneous strain rate over a period of 7.5 Ma, commonly considered to be the age of the initiation of intraplate deformation. Royer & Gordon's finite motion was initially given on a 11 Ma basis, but they now acknowledge that most of the deformation has occurred during the last 7.5–8 Myr (DeMets *et al.* 2005). Although the timing of deformation now seems to be well established, the published estimations of the finite deformation are quite variable, depending on the authors and the methods used. Shortening estimates on the PHEDRE line ranges from 22–37 to 36–62 km, the highest bounds being obtained by assuming a contribution of the seismically undetected small faults of 40 per cent (Chamot-Rooke *et al.* 1993). Van Orman *et al.* (1995) stay on the lower bound of the estimate along the PHEDRE line arguing to negligible contribution of the small faults. They also propose 11 ± 2 km on the Conrad line 300 km west of PHEDRE line. Jestin (1994) quotes shortenings of 26–43 km (43–71 km upper bound if small faults are included) on a line run about

300 km east of the PHEDRE reference line. The latter estimates are minimum since the line does not cross the entire deformation zone (line 2 in Chamot-Rooke *et al.* (1993)). The amount of shortening deduced from plate reconstructions (DeMets *et al.* 2005) exceeds the shortenings measured on the westernmost seismic line (29 km versus 11 km), but is within the estimates made on the PHEDRE line (Table 9). Our new estimations based on the IN/AU instantaneous pole of rotation (27 ± 9 on the westernmost line and 36 ± 9 on the PHEDRE line) are close to the plate reconstruction estimates (29 ± 2 and 42 ± 2, respectively). We see two limitations to these comparisons. First, DeMets *et al.* (2005) mention a widespread extension event prior to compression. Although this event remains undetected on the seismic lines, it may have biased the estimation of finite compressive deformation on the profiles. The second limitation is the use of the rigid plate motion to infer the amount of shortening to be accommodated within the diffuse deforming zone.

Our second estimation is based on the predicted moment rates previously discussed (Table 6). Strain rates are back calculated from the moment rates at a regional scale (the five regions described previously), assuming that the strain rate principal axis is

Table 8. Finite strain (in km) estimated from observed and predicted moment rates extrapolated over 7.5 Ma.

Regions:	1[a] (WB)	2 (South CIB)	3 (central CIB)	4 (north CIB)	5 (Chagos)
Style:	Shear	Compression	Compression	Compression	Extension
Historical seismicity	47.3	−0.0	−10.9	−0.0	26.4
Non-uniform—heat flow	109.2	−16.7	−39.6	−9.8	12.3
Non-uniform—age	141.1	−37.7	−15.0	−7.0	33.7
Uniform—anisotropic	89.5	−16.7	−13.5	−29.4	20.8

A simplified fault geometry is used to back calculate strain rates. In the three regions of the CIB (regions 2, 3 and 4), thrust faults are assumed to strike E–W with a 45° dip angle. Using Kostrov formulation, we extract the N–S principal strain rate. Similarly, region 5 (Chagos Laccadive) has E–W striking normal faults and the obtained strain rate is also N–S oriented. In the case of the WB (region 1), N–S vertical faults are considered to compute the shear strain rate there. A characteristic length L is determined in each region in the direction of deformation to compute corresponding extrapolated finite motions. $d = \epsilon_L \cdot L \cdot \Delta t$ where $\Delta t = 7.5$ Myr. For regions 2, 3, 4 and 5 the considered direction is N–S and $L = 1300$ km, 1000 km, 1300 and 1300 km, respectively, since we want to obtain the finite N–S shortening or the finite N–S extension.
[a]In region 1, we assume that all the deformation is accommodated by N–S strike-slip faults. Shear displacement is then calculated considering a shear band width extending from the NyR to the Investigator Fracture Zone (1300 km width). $L = \frac{\text{WB area}}{\text{shear band width}} \cdot \cdot$

Table 9. Baseline shortenings.

Baseline	Length (km)	Motion (km)	Strain rate (10^{-16} s^{-1})	Finite motion (km)
B1: WB	4391	−103.5 ± 9.1	−1.00 ± 0.09	−125 ± 28[a]
B2: CIB	3002	−45.0 ± 10.3	−0.64 ± 0.15	−48 ± 9[a]
B3: Chagos	1112	12.5 ± 9.7	0.48 ± 0.37	20 ± 4[a]
B4: CIB	2113	−36.2 ± 9.4	−0.73 ± 0.19	−22 to −37[b] (−41.7 ± 2.4 km)[d]
B5: CIB	1279	−26.6 ± 9.3	−0.88 ± 0.31	−11 ± 2[c] (−28.7 ± 2.2 km)[d]

[a]Royer & Gordon (1997) (estimated from finite India/Capricorn motion).
[b]Chamot-Rooke *et al.* (1993).
[c]Van Orman *et al.* (1995) (estimated from faulting).
[d]DeMets *et al.* (2005) (estimated from finite India/Capricorn motion).
Our shortening values and uncertainties (2σ errors) are derived from the India/Australia pole, as we consider that extremities of all baselines are on rigid plates.

perpendicular to 45° dipping faults (or at 45° of vertical strike slip faults). Table 8 shows the results for region 1 to region 5, for every model but the isotropic one. These shortening values now corresponds to the true outputs of our models since they do not require any kind of rigid plate approximation. For all models, the mean total shortening in the CIB is ∼60 km (between longitudes 74°E to 88°E). This is obviously exaggerated for the westernmost line, but still within the upper bound for the two PHEDRE lines quoted above. The total amount of shear in the WB is very large, especially for the two non-homogeneous models (∼110 km and ∼140 km for the heat flow model and age model, respectively). No direct comparison can be made since finite shear has not been estimated yet. However, B1 baseline shortening for our best model is within the bounds of the predicted finite motion from plate reconstructions (Table 9). These numbers tend to suggest a continuum of deformation since 7.5 Ma. However, error bars on the various estimates are quite large, and we cannot totally rule out spatial and temporal variations in the rate of deformation (Krishna *et al.* 2001).

5.4 Regional kinematics and dynamics

We show in Figs 12 and 13 the modelled velocity field in an Australia and India reference frame, respectively. In the Indian reference frame, we see that residuals are small down to 5° N, in particular, west of the NyR. Far east of the NyR, the velocity field shows Australia moving ∼30 mm yr^{-1} northward, decreasing to ∼10 mm yr^{-1} towards the NyR, then vanishing across the ridge as a result of

left-lateral strike slip along its northern portion. The velocity vector along the trench with respect to India is always roughly N–S, but gradually decreases from SE to NW (Fig. 13). This implies that motion along the Sumatra trench is neither purely Australian nor purely Indian (Vigny *et al.* 2005). Velocity at 8° S, 105.5°E (Sunda Strait) is 17 mm yr^{-1} with azimuth N1°E and velocity is still 8 mm yr^{-1} with azimuth N10°E at 4°N, 95°E near the Aceh December 2004 megathrust earthquake (velocities are given with respect to India). Using the Sunda/India rotation pole of Socquet *et al.* (2006) (20.2°N, 26.1°E, 0.370° Myr^{-1}), we compute predicted convergence motions for the two previous locations: 57 mm yr^{-1} towards N16°E near the Sunda Strait and 46 mm yr^{-1} towards N18°E near the Aceh megathrust erthquake epicentre. The kinematics that we reach is obviously the result of the complex interaction of the various forces applied to the India–Australia Plate. Previous mechanical models emphasized the role of Indian ridges push, Himalayan resistance and slab pull at Sunda trenches (Cloetingh & Wortel 1986; Coblenz *et al.* 1998). The comparison of our instantaneous motion with the recent reconstructions of India-Australia relative motion through time suggests that the intraplate velocity field remained more or less constant since the time of initiation around 7.5–8 Ma. If not, the agreement between extrapolated instantaneous shortening (obtained from GPS and earthquakes) and finite shortening (obtained from magnetic anomalies and seismic lines) would be difficult to explain.

Our modelled deformation field can thus be seen as deriving from a velocity perturbation added to the overall motion of the India–Australia Plate as a result of external extra forces applied either at

Table 10. Finite and instantaneous India/Australia rotation poles with their 1σ uncertainties.

Study	Period	Latitude	Longitude	ω (° Myr^{-1})	σ_ω	Semimaj. axis	Semimin. axis	az.
Nuvel1A	0–3.02 Ma	−5.6	77.1	−0.300	0.074	7.4°	3.1°	43°
(DeMets *et al.* 2005)[c]	0–7.86 Ma	−4.9	73.1	−0.318	0.036	3.9°	1.5°	39°
(DeMets *et al.* 1994b)	0–3.02 Ma	−3.2	75.1	−0.305	0.028	2.5°	1.2°	43°
(Tinnon *et al.* 1995)[a]	0–100 yr	−10.1	81.5	−0.100	0.060	9.1°	5.4°	0°
This study[a]	0–100 yr	−21.0	81.3	−0.064	0.020	11.9°	4.2°	−3°
This study[b]	0–100 yr	−11.27	72.8	−0.310	0.012	3.2°	0.8°	11.5°
(Kreemer *et al.* 2003)[b]	0–100 yr	−5.2	70.5	−0.398	0.019	0.8°	0.8°	25°
(Socquet *et al.* 2006)	0–10 yr	−6.6	73.7	−0.397	0.028	3.3°	0.73°	11.3°.

[a]Seismicity.
[b]Seismicity and GPS.
[c]Capricorn/India motion.
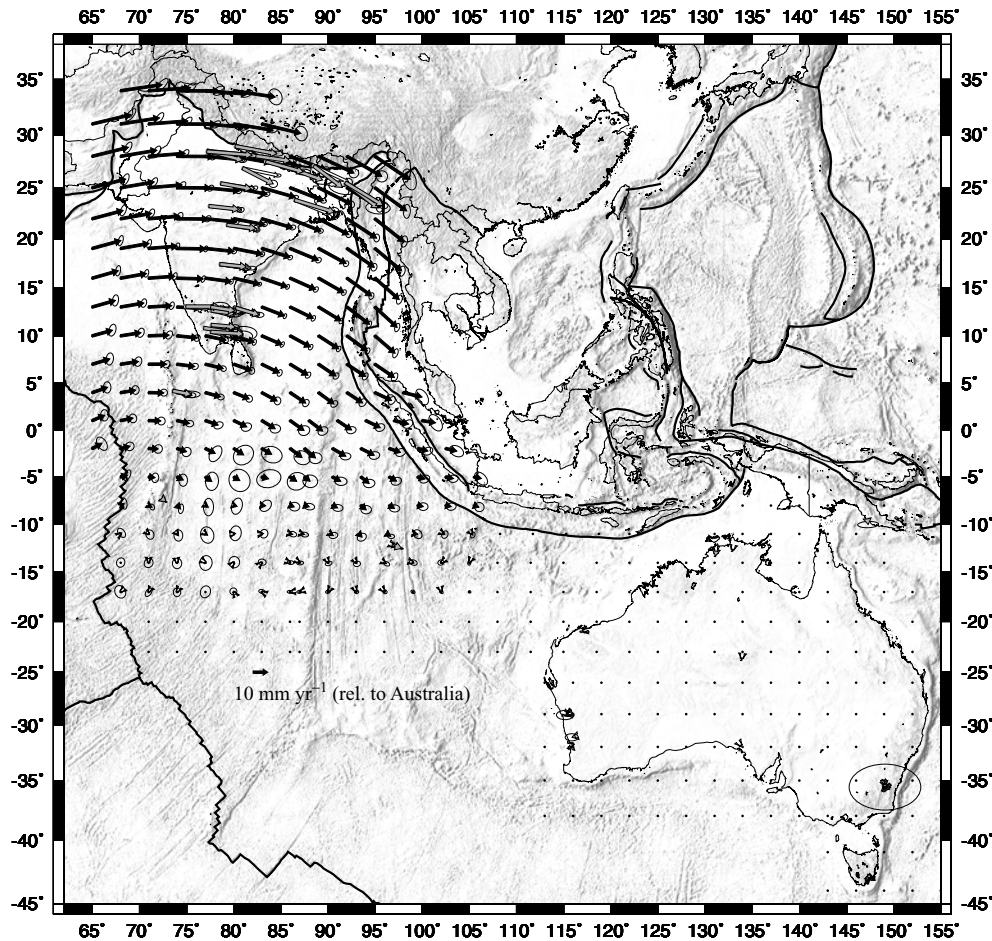
Figure 12. Modelled velocity field obtained from our preferred model in the Australian reference frame. Continental India is moving 13 mm yr^{-1} to 26 mm yr^{-1} eastward with respect to Australia. Error ellipses are 1σ.

the boundaries of the plate, or possibly below it (Ghosh *et al.* 2006). Although purely kinematic, our model gives some insight on the origin of these forces. The dynamic interpretation is totally different whether the perturbation resulted from a change of Australia motion or a change of India motion. A quite intuitive model is one in which India slows down as a result of the resistance to subduction of the Indian continent, thus triggering intraplate deformation. If Australia motion remained unchanged, then the new velocity field established at the onset of the intraplate deformation is the one obtained in the Australian frame of reference (Fig. 12). In this reference frame, In-

dia is moving due east with a velocity bracketed between 13 and 26 mm yr^{-1}. Such a change in the motion of India would be surprising for two reasons: first, a sudden eastward motion of India is difficult to understand in the framework of the Himalayan chain building. Second, India motion with respect to Eurasia does not seem to have changed in direction since anomaly 6 (21 Ma) (Patriat & Achache 1984) and DeMets *et al.* (2005) did not detect any change of motion with respect to Somalia before and after anomaly 4n2 (7.86 Ma). An exclusively 'Indian driven' deformation is thus quite implausible.
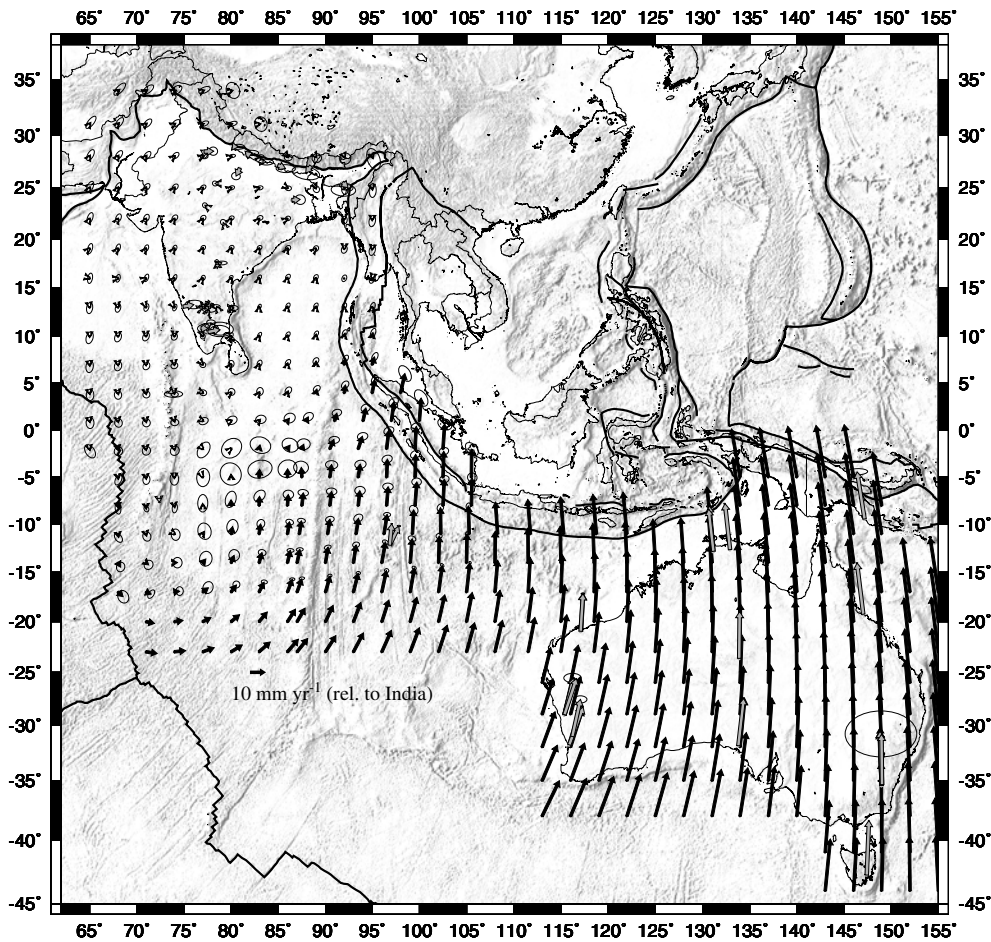
Figure 13. Modelled velocity field obtained from our preferred model in the Indian reference frame. It shows continental Australia moving $\sim$30 mm yr^{-1} northward with respect to India. Error ellipses are 1σ.

The alternative is that Australia motion did change, but India motion did not, at least in direction. A first end-member model is one in which the motion of India remained unchanged at the onset of deformation: extra motion is thus directly obtained by recasting the velocity field in an Indian frame of reference (Fig. 13). In this frame, Australia is moving more or less to the north. Notice that in that case, the extra motion is normal to the trenches along a sizeable portion of the northern Australian plate boundary, from the far East (Banda and New Guinea) to the Sunda Strait. Of course, the exact shape of the subduction may have been different at the time of initiation of the intraplate deformation, but the net result of the Australian velocity field is an increase of the subduction velocity along all east-west trending portions of trench. The velocity field also adds a significant shear component on north-south segments, in particular, on the Sumatra-Andaman. This would provide a simple explanation for the close relationship in time of a series of important tectonic changes: intraplate deformation in the Indian Ocean (post 8 Ma, Cochran 1990), initiation of the Great Sumatra fault (post 5 Ma, Sieh & Natawidjaja 2000), and latest pulse of oceanic accretion in the Andaman Basin (post 5 Ma, Chamot-Rooke *et al.* 2001).

A hybrid model is one in which the velocity field is perpendicular both to the Australian subductions and to the Himalayan front. Such a reference frame actually exists, and implies deceleration of India along its subduction-collision direction (about 10 mm yr^{-1}) and a simultaneous northward acceleration of Australia (about 10–

20 mm yr^{-1}). This leaves open the possibility of a decrease of India convergence rate, the GPS motion being significantly slower than the Nuvel1A motion (Paul *et al.* 2001; Kreemer *et al.* 2003; Vigny *et al.* 2003).

An important output of our model is that northward acceleration of Australia, with or without change in the rate of India motion, is a plausible mechanism for the initiation of the intraplate deformation. Australia has been dragged northward through time by the old Indian oceanic slab engaged into the subductions. Motion with respect to Eurasia was large prior to India collision (pre-45 Ma) and then dropped to about 50 mm yr^{-1}. At the time of intraplate deformation, Australia detached from India under the combined effect of Australia/Antarctica ridge push and slab pull. Our velocity field suggests that this occurred along a long line of weakness: the NyR and fractures zones east of it. The time lag between the early signs of collision and initiation of intraplate deformation (lag of about 35 Ma) is best explained in terms of a sudden event, Australia being liberated from its Indian 'brake'. The detachment is however not fully achieved, and deformation still involves a broad area.

6 CONCLUSION

(i) Combining horizontal motion obtained by repeated GPS measurements with the style of deformation derived from focal

mechanisms of earthquakes is a balanced way to derive an instantaneous strain-rate field and its associated velocity field in actively deforming areas (Haines & Holt 1993). We show that GPS and earthquakes data are complementary in the case of the intraplate deformation of the India–Australia Plate: GPS velocities provide far field as well as within plate constraints, whereas focal mechanisms strongly constrain the *a priori* style of deformation, but not the amplitude.

(ii) The best strain field—in terms of GPS vector fitting and distribution and style of the deformation—is obtained when introducing in the modelling heat-flow related weakening of the oceanic lithosphere. We show that the observed present-day deformation concentrates at places where surface heat-flow is high. The lithosphere is weak not only where it is young, such as in the northern WB, but also in a broad region around the Afanasy Nikitin hotspot trace. Conversely, the oldest parts of the Indian Ocean lithosphere are less deforming: more rigid portions cover the Cretaceous oceanic domain, that is, the northern CIB and the Bay of Bengal. Although we allow for deformation of continental India throughout our modelling, severe deformation of the continent is not required, with the noticeable exception of the Shillong plateau.

(iii) The boundary role played by NyR is confirmed (Tinnon *et al.* 1995; Deplus *et al.* 1998). Deformation style abruptly changes from north-south shortening with little shearing west of the ridge to strong left-lateral shearing east of it. Maximum shear is localized along the central and northern portions of the ridge. The area between the NyR and the Sumatra Trench is presently a wide (several hundreds km) oceanic left lateral shear band. Our estimation of total amount of shear accommodated there since the beginning of deformation (7.5–8 Ma) is at least 100 km. A sizeable portion of the Sumatra-Andaman subduction zone is within the deforming zone. Intraplate deformation is actually maximum in the region of initiation of the 2004 Sumatra megathrust earthquake. The implication is that the subduction motion at that trench is neither fully Australian nor fully Indian. Using our intraplate velocity field together with recent India-Sunda motion determination, we find that the predicted convergence motion at the megaearthquake epicentre is 46 mm yr^{-1} towards N18°E.

(iv) The baseline shortenings obtained from our instantaneous model across the diffuse boundary zone are in good agreement with shortenings from finite deformation using magnetic data and faulting data from seismic profiles. This suggests a continuum of deformation since the onset of intraplate deformation. The introduction of a Capricorn plate is not required, because the motion of this microplate cannot be detected by the type and distribution of data we use.

(v) Examining our solution in different reference frames, we find that an exclusively Indian driven mechanism for the intraplate deformation is implausible. We suggest that deformation initiated when Australia started to detach from India along the NyR weakness line—as a combine result of slab pull at Sunda trenches and push at the Southeast Indian Ridge—and that this process is still at work today. The net effect was an acceleration of Australia subduction. Significant change in India convergence direction or rate is not required.

REFERENCES

Abercrombie, R.E., Antolik, M. & Ekstrom, G., 2003. The June 2000 Mw 7.9 earthquakes south of Sumatra: deformation in the India-Australia Plate, *J. geophys. Res.,* **108,** 2018–2034.

Banerjee, P., 2005. Inter-seismic geodetic motion and far-field coseismic surface displacements caused by the 26 December 2004 Sumatra earthquake observed from GPS data, *Curr. Sci.,* **88,** 1491–1496.

Beavan, J. & Haines, J., 2001. Contemporary horizontal velocity and strain rate fields of the Pacific-Australian plate boundary zone through New Zealand, *J. geophys. Res.,* **106,** 741–770.

Bergman, E.A. & Solomon, S.C., 1984. Source mechanisms of earthquakes near mid-ocean ridges from body waveform inversion: implications for the early evolution of oceanic lithosphere, *J. geophys. Res.,* **89,** 11 415–11 441.

Bergman, E.A. & Solomon, S.C., 1985. Earthquake source mechanisms from body-waveform inversion and intraplate tectonics in the northern Indian Ocean, *Phys. Earth planet. Inter.,* **40,** 1–23.

Bergman, E.A., Nabelek, J.L. & Solomon, S.C., 1984. An extensive region of off-ridge normal faulting earthquakes in the southern Indian Ocean, *J. geophys. Res.,* **89,** 2425–2443.

Bilham, R. & England, E., 2001. Plateau 'pop up' in the great 1897 Assam earthquake, *Nature,* **410,** 806–809.

Bilham, R., Bendick, R. & Wallace, K., 2003. Flexure of the Indian plate and intraplate earthquakes, *Proc. Indian Acad. Sci (Earth planet. Sci.),* **112,** 315–329.

Biswas, S. & Majumdar, R.K., 1997. Seismicity and tectonics of the Bay of Bengal: evidence for intraplate deformation in the northern Indian plate, *Tectonophysics,* **269,** 323–336.

Bull, J.M., 1990. Structural style of intraplate deformation, Central Indian Ocean basin: evidence for the role of the fracture zones, *Tectonophysics,* **184,** 213–228.

Bull, J.M. & Scrutton, R.A., 1992. Seismic reflection images of intraplate deformation, Central Indian Ocean, and their tectonic significance, *J. Geol. Soc. Lond.,* **149,** 955–966.

Carslaw, H.S. & Jaeger, J.C., 1959. *Conduction of Heat in Solids*, Oxford University Press, New York, 510 pp.

Chamot-Rooke, N. & Le Pichon, X., 1989. Zenisu Ridge: a mechanical model of formation., *Tectonophysics,* **160,** 175–193.

Chamot-Rooke, N., Jestin, F., De Voogd, B. & the Phèdre Working Group, 1993. Intraplate shortening in the central Indian Ocean determined from 2100-km-long north-south deep seismic reflection profile, *Geology,* **21,** 1043–1046.

Chamot-Rooke, N., Rangin, C. & Nielsen C., 2001. Timing and kinematics of Andaman basin opening, *EOS, Trans. Am. geophys. Un.,* **82**(20), Spring meet. Suppl., Abstract T42B-08.

Cloetingh, S.A.P.L. & Wortel, M.J.R., 1985. Regional stress in the Indian plate, *Geophys. Res. Lett.,* **12,** 77–80.

Cloetingh, S.A.P.L. & Wortel, M.J.R., 1986. Stress in the Indo-Ausralian plate, *Tectonophysics,* **132,** 49–67.

Coblenz, D.D., Zhou, S., Hillis, R.R. and Richardson, R.M. & Sandiford, M., 1998. Topography, boundary forces, and the Indo-Australian intraplate stress field, *J. geophys. Res.,* **103,** 919–931.

Cochran, J.R., 1990. Himalayan uplift, sea level, and the record of Bengal Fan sedimentation at the ODP LEG 116 Sites, *Proceedings of the Ocean Drilling Program, Scientific Results,* **116,** 397–414.

Cochran, J.R. *et al.,* 1989. *Proc. ODP, Init. Repts.*, **116**: College Station, TX (Ocean Drilling Program).

Chandra, U., 1977. Earthquakes of Peninsular India—A seismotectonic study, *Bull. seism. Soc. Am.,* **67,** 1387–1413.

Chen, W.P. & Molnar, P., 1990. Source parameters of earthquakes and intraplate deformation beneath the Shillong Plateau and the northern Indoburman Ranges, *J. geophys. Res.,* **95,** 12 527–12 552.

Delescluse, M. & Chamot-Rooke, N., 2006. Heat flow in the deforming Indian oceanic lithosphere, *Geophys. Res. Abs.,* **8,** 07 584.

DeMets, C., Gordon, R.G. & Argus, D.F., 1988. Intraplate deformation and closure of the Australia-Antarctica-Africa plate circuit, *J. geophys. Res.,* **93,** 11 877–11 897.

DeMets, C., Gordon, R.G., Argus, D.F. & Stein, S., 1990. Current plate motions, *Geophys. J. Int.,* **101,** 425–478.

DeMets, C., Gordon, R.G., Argus, D.F. & Stein, S., 1994a. Effect of recent revisions of the geomagnetic reversal time scale on estimate of current plate motions, *Geophys. Res. Lett.,* **21,** 2191–2194.

DeMets, C., Gordon, R.G. & Vogt, P., 1994b. Location of the Africa-Australia-India triple junction and motion between the Australian and Indian plates: results from an aeromagnetic investigation of the Central Indian and Carlbergs ridges, *Geophys. J. Int.,* **119,** 893–930.

DeMets, C., Gordon, R.G. & Royer J.Y., 2005. Motion between the Indian, Capricorn and Somalian plates since 20 Ma: implications for the timing and magnitude of distributed lithospheric deformation in the equatorial Indian ocean, *Geophys. J. Int.,* **161,** 445–468.

Deplus, C., 2001. Indian Ocean Actively Deforms, *Science,* **292,** 1850–1851.

Deplus, C. *et al.*, 1998. Direct evidence of active deformation in the eastern Indian oceanic plate, *Geology,* **26,** 131–134.

Engdahl, E.R., Van Der Hilst, R.D. & Buland, R.P., 1998. Global teleseismic earthquake relocation with improved travel times and procedures from depth determination, *Bull. seism. Soc. Am.,* **88,** 722–743.

Geller, C.A., Weissel, J.K. & Anderson, R.N., 1983. Heat transfer and intraplate deformation in the Central Indian Ocean, *J. geophys. Res.,* **88,** 1018–1032.

Ghosh, A., Holt, W.E., Flesch, L.M. & Haines A.J., 2006. Gravitational potential energy of the Tibetan Plateau and the forces driving the Indian plate, *Geology,* **34,** 321–324.

Gordon, R.G., DeMets, C. & Argus, D.F., 1990. Kinematic constraints on distributed lithospheric deformation in the equatorial indian ocean from present motion between the Australian and Indian plates, *Tectonics,* **9,** 409–422.

Haines, A.J. & Holt, W.E., 1993. A procedure for obtaining the complete horizontal motions within zones of distributed deformation from the inversion of strain rate data, *J. geophys. Res.,* **98,** 12 057–12 082.

Haines, A.J., Jackson, J.A. & Holt, W.E., 1998. Representing distributed deformation by continuous velocity field, *Inst. of Geol. and Nucl. Sci.,* **98/5,** Sci. Rept., Wellington, New Zealand.

Heflin *et al.* (2004.2). January 1, 2004 (date of solution). July 2006 (last viewed). GPS time series. http://sideshow.jpl.nasa.gov/mbh/series.html.

Hetényi, G., Cattin, R., Vergne, J. & Nabelek, J.L., 2006. The effective elastic thickness of the India Plate from receiver function imaging, gravity anomalies and thermo-mechanical modelling, *Geophys. J. Int.,* in press, doi:10.1111/j.1365-246X.2006.03198.x.

Holt, W.E. & Haines, A.J., 1995. The kinematics of northern South Island New Zealand determined from geologic strain rates, *J. geophys. Res.,* **100,** 17 991–18 010.

Holt, W.E., Li, M. & Haines, A.J., 1995. Earthquake strain rates and instantaneous relative motions within central and eastern Asia, *Geophys. J. Int.,* **122,** 569–593.

Holt, W.E., Shen-Tu, B., Haines, J. & Jackson, J., 2000. On the determination of self-consistent strain rate fields within zones of distributed deformation, in *The History and Dynamics of Global Plate Motions*, pp. 113–141, eds Richards, M.A., Gordon, R.G. & Van Der Hilst, R.D., AGU, Washington, DC.

Jestin, F., 1994. Cinématique rigide et déformations dans la jonction triple Afar et dans le Bassin Indien Central, Université Paris VI, *PhD thesis,* 217 pages.

Karner, G.D. & Weissel, J.K., 1990. Factors controlling the location of compressional Deformation of Oceanic Lithosphere in the Central Indian Ocean, *J. geophys. Res.,* **95,** 19 795–19 810.

Kostrov, V.V., 1974. Seismic moment, and energy of earthquakes, and the seismic flow of rock (in Russian), *Izv. Acad. Sci. USSR Phys. Solid Earth,* **1,** 23–44.

Kreemer, C., Holt, W.E. & Haines, A.J., 2003. An integrated gobal model of present-day plate motions and plate boundary deformation, *Geophys. J. Int.,* **154,** 1–27.

Krishna, K.S., 2003. Structure and evolution of the Afanasy Nikitin seamount, buried hills and 85E Ridge in the northeastern Indian Ocean, *Earth planet. Sci. Lett.,* **209,** 379–394.

Krishna, K.S. & Gopala Rao, D., 2000. Abandoned Paleocene spreading center in the northeastern Indian Ocean: evidence from magnetic and seismic reflection data, *Mar. Geol.,* **162,** 215–224.

Krishna, K.S., Ramana, M.V., Gopala Rao, D., Murthy, K.S.R., Malleswara Rao, M.M., Subrahmanyam, V. & Sarma, K.V.L.N.S., 1998. Periodic deformation of oceanic crust in the central Indian ocean, *J. geophys. Res.,* **103,** 17 859–17 875.

Krishna, K.S., Bull, J.M. & Scrutton, R.A., 2001. Evidence for multiphase folding of the Central Indian Ocean lithosphere, *Geology,* **29,** 715–718.

Lachenbruch, A.H. & Sass, J.H., 1980. Heat flow and energetics of the San Andreas fault zone, *J. geophys. Res.,* **85,** 6185–6223.

Lachenbruch, A.H. & Sass, J.H., 1992. Heat flow from Cajon Pass, Fault Strength, and Tectonic Implications, *J. geophys. Res.,* **97,** 4995–5015.

Le Pichon, X., 1968. Sea-floor spreading and continental drift. *J. geophys. Res.,* **73,** 3661–3697.

Minster, J.B. & Jordan, T.H., 1978. Present Day Plate Motions, *J. geophys. Res.,* **83,** 5331–5354.

Muller, R.D., Roest, W.R., Royer, J.Y., Gahagen, L.M. and Sclater, J.G., 1997. Digital isochrons of the ocean floor, *J. geophys. Res.,* **102,** 3211–3214.

Pancha, A., Anderson, J.G. & Kreemer, C., 2006. Comparison of seismic and geodetic scalar moment rates across the Basin and Range province, *Bull. seism. Soc. Am.,* **96,** 11–32.

Patriat, P. & Achache, J., 1984. India-Eurasia collision chronology has implication for crustal shortening and driving mechanism of plates, *Nature,* **311,** 615–621.

Paul, J., Singh, R.N., Subrahmanyam, C. & Drolia, R.K., 1990. Emplacement of Afanasy-Nikitin seamount based on transfer function analysis of gravity and bathymetry data, *Earth planet. Sci. Lett.,* **96,** 419–426.

Paul, J. *et al.*, 2001. The motion and active deformation of India, *Geophys. Res. Lett.,* **28,** 647–650.

Petroy, D.E. & Wiens, D.A., 1989. Historical seismicity and implications for diffuse plate convergence in the northeast Indian Ocean, *J. geophys. Res.,* **94,** 12 301–12 319.

Pollack, H.N., Hurter, S.J. & Johnson, J.R., 1993. Heat flow from the earth's interior: analysis of the global data set, *Rev. Geophys.,* **31**(3), 267–280.

Royer, J.Y. & Gordon, R.G., 1997. The Motion and Boundary Between the Capricorn and Australian Plates, *Science,* **277,** 1268–1274.

Royer, J.Y., Peirce, J.W. & Weissel, J.K., 1991. Tectonic constraints on the Hot-Spot formation of Ninetyeast Ridge, *Proceedings of the Ocean Drilling Program, Scientific Results,* **121,** 763–776.

Savage, J.C. & Simpson, R.W., 1997. Surface strain accumulation and the seismic moment tensor, *Bull. seism. Soc. Am.,* **87,** 1345–1353.

Sieh, K. & Natawidjaja, D., 2000. Neotectonics of the Sumatran fault, Indonesia, *J. geophys. Res.,* **105,** 28 295–28 326.

Socquet, A., 2003. Accommodation du Mouvement Relatif entre l'Inde et la Sonde, Université Paris XI, *PhD thesis*, 195 p.

Socquet, A., Vigny, C., Chamot-Rooke, N., Simons, W., Rangin, C. & Ambrosius, B., 2006. India and Sunda plates motion and deformation along their boundary in Myanmar determined by GPS, *J. geophys. Res.,* **111,** B05406. doi:10.1029/2005JB003877.

Stein, S. & Okal, E.A., 1978. Seismicity and tectonics of the Ninetyeast Ridge area: evidence for internal deformation of the Indian Plate, *J. geophys. Res.,* **83,** 2233–2246.

Stein, C.A. & Weissel J.K., 1990. Constraints on the Central Indian Basin thermal structure from heat flow, seismicity and bathymetry, *Tectonophysics,* **176,** 315–332.

Tinnon, M.J., Holt, W.E. & Haines, A.J., 1995. Velocity gradients in the northern Indian Ocean inferred from earthquakes moment tensors and relative plate velocities, *J. geophys. Res.,* **83,** 24 315–24 329.

Triep, E.G. & Sykes, L.R., 1997. Frequency of occurence of moderate to great earthquakes in intracontinental regions: implications for changes in stress, earthquake prediction, and hazards assessments, *J. geophys. Res.,* **102,** 9923–9948.

Van Orman, J., Cochran, J.R., Weissel, J.K. & Jestin, F., 1995. Distribution of shortening between the Indian and Australian plates in the central Indian Ocean, *Earth planet. Sci. Lett.,* **133,** 35–46.

Verzhbitsky, E.V. & Lobkovsky, L.I., 1993. On the mechanism of heating up of the Indo-Australian Plate, *J. Geodyn.,* **17,** 27–38.

Vigny, C., Socquet, A., Rangin, C., Chamot-Rooke, N., Pubellier, M., Bouin, M.N., Bertrand, G. & Becker, M., 2003. Present-day crustal deformation around Sagaing fault, Myanmar, *J. geophys. Res.,* **108,** Art. No 2533.

Vigny, C. *et al.*, 2005. Insight into the 2004 Sumatra-Andaman earthquake from GPS measurements in southeast Asia, *Nature,* **436,** 201–206.

Watts, A.B., Steckler, M.S. & Bodine, J.H., 1980. Observations of flexure and state of stress in the oceanic lithosphere, *J. geophys. Res.,* **85,** 6369–6376.

Weissel, J.K., Anderson, R.N. & Geller, C.A., 1980. Deformation of the Indo-Australian plate, *Nature,* **287,** 284–291.

Wessel, P. & Smith, W.H.F., 1995. New version of the Generic Mapping Tools released, *EOS, Trans. Am. geophys. Un.,* **76**(33), 329.

Wiens, D.A., 1986. Historical seismicity near Chagos: a complex deformation zone in the equatorial Indian Ocean, *Earth planet. Sci. Lett.,* **76,** 350–360.

Wiens, D.A. & Stein, S., 1984. Intraplate seismicity and stresses in young oceanic lithosphere, *J. geophys. Res.,* **89,** 11 442–11 464.

Wiens, D.A. *et al.*, 1985. A diffuse plate boundary model for Indian Ocean tectonics, *Geophys. Res. Lett.,* **12,** 429–432.